Available online at www.sciencedirect.com

ScienceDirect

Geochimica et Cosmochimica Acta 324 (2022) 117–139

Geochimica et Cosmochimica Acta

www.elsevier.com/locate/gca

# Controls of REY enrichment in the early Cambrian phosphorites

Hongjie Zhang [a,c], Haifeng Fan [a,c,*], Hanjie Wen [b,c], Tao Han [a,c], Ting Zhou [a,c], Yong Xia [a,c]

[a] State Key Laboratory of Ore Deposit Geochemistry, Institute of Geochemistry, Chinese Academy of Sciences, Guiyang 550081, China
[b] School of Earth Sciences and Resources, Chang'an University, Xi'an 710054, China
[c] University of Chinese Academy of Sciences, Beijing 100049, China

Received 29 June 2021; accepted in revised form 2 March 2022; available online 8 March 2022

**Abstract**

Rare earth elements and Yttrium (REYs) are critical to the emerging high-tech and green-energy industries, generating tremendous REY demand in recent decades. Recently, many sedimentary phosphorites have been reported to have extraordinary REY enrichment (> 1000 ppm) and may become new REY resources. However, the controls of REY enrichment in phosphorites have not been well constrained. To better understand the discrepant REY enrichment in phosphorites, the early Cambrian high-REY Zhijin (ZJ) phosphorites (~500–2000 ppm) and the relatively low-REY Meishucun (MSC, ~200–400 ppm) and Xia'an (X'A, mostly < 200 ppm) phosphorites on the Yangtze Block of South China were investigated with mineralogy, bulk-rock elements, total organic carbon, in-situ elements, and Zn-Fe isotopes. The mineral characteristics, REY indexes, and in-situ REY mapping indicate that the X'A phosphorites may represent pristine phosphorites, whereas the ZJ and MSC phosphorites may have experienced intensive diagenetic alteration. Diagenetic alteration can only explain the REY enrichment in the MSC phosphorites compared to the pristine X'A phosphorites, but it does not sufficiently explain the extraordinary REY enrichment in the ZJ phosphorites. Additionally, the lower $\delta^{66}Zn$ values of the ZJ and X'A phosphorites ($\delta^{66}Zn_{average}$ = 0.16‰ and 0.14‰, respectively) than those of the MSC phosphorites ($\delta^{66}Zn_{average}$ = 0.75‰) indicate higher productivity levels in the ZJ and X'A areas. However, the high-productivity X'A phosphorites yielded very low REY concentrations, indicating that the extraordinary REY enrichment in the ZJ phosphorites cannot be ascribed to high productivity levels. Notably, the ZJ phosphorites may have experienced more intensive Fe redox cycling under fluctuating oxic–suboxic deposition conditions (~0.0‰–0.45‰ $\delta^{56}Fe$ values in near-pure phosphorites) than the MSC and X'A phosphorites with completely oxic deposition conditions (~0.0‰ $\delta^{56}Fe$ values). Frequent Fe redox cycling can greatly enrich REYs in porewater, which can be subsequently transferred into francolites during its formation and early diagenesis. Therefore, frequent Fe redox cycling driven by fluctuating oxic–suboxic seawater conditions may be responsible for the extraordinary REY enrichment in the ZJ phosphorites. If this is the case, we propose that phosphorites deposited near the oxic–suboxic redox chemocline are favorable for extraordinary REY enrichment, such as the coeval near-slope phosphate concretions on the Yangtze Block and other phosphorites or phosphatic rocks formed in different basins at different geological times.


*Keywords:* In-situ REY mapping; Zn-Fe isotopes; Diagenetic REY uptake; Productivity levels; Fe redox cycling

## 1. INTRODUCTION

Rare earth elements and Yttrium (REYs) are particularly important for the emerging high-tech and green-energy industries, inducing tremendous REY demand that

* Corresponding author at: State Key Laboratory of Ore Deposit Geochemistry, Institute of Geochemistry, Chinese Academy of Sciences, Guiyang 550081, China.
*E-mail address:* fanhaifeng@mail.gyig.ac.cn (H. Fan).

https://doi.org/10.1016/j.gca.2022.03.003
0016-7037/

is quickly outstripping the known supply in recent decades (Binnemans et al., 2018; Balaram, 2019). Currently, the world's REYs are supplied predominantly by carbonatite deposits and ion-adsorption type deposits; the former mainly output light REYs (LREYs; La-Nd), whereas the latter are major sources of middle REYs (MREYs; Sm-Dy) and heavy REYs (HREYs; Ho-Lu and Y) (Kynicky et al., 2012; Hoshino et al., 2016). Relatively, MREYs and HREYs are exposed to higher supply risks than LREYs because ion-adsorption type deposits are typically small and low grade (Kynicky et al., 2012; Hoshino et al., 2016). Therefore, many researchers have attempted to explore new MREY and HREY resources (Kato et al., 2011; Emsbo et al., 2015; Hoshino et al., 2016). For example, modern deep-sea muds have been found to be extremely REY-enriched (~1000–2000 ppm) (particularly MREYs and HREYs) (Kato et al. 2011; Yasukawa et al., 2014).

Notably, many sedimentary phosphorites have been found to have extraordinary REY enrichment (> 1000 ppm) (particularly MREYs and HREYs). Phosphorites with extraordinary REY enrichment have been reported worldwide and throughout most of the geological history (Awadalla, 2010; Chen et al., 2013; Gómez-Peral et al., 2014; Emsbo et al., 2015; Joosu et al., 2015, 2016; Francovschi et al., 2020), indicating tremendous REY resource potential. For example, Emsbo et al. (2015) showed that the phosphorite-type REY resources in the United States are comparable to China's ion-adsorption type REY resources. However, the origin of extraordinary REY enrichment in phosphorites has not been well constrained. In previous studies, continental input, hydrothermal activity, weathering processes, early diagenesis, biological activity, and seawater redox conditions have all been proposed as possible controls, but many controversies remain (Watkins et al., 1995; Gnandi and Tobschall, 2003; Haley et al., 2004; Chen et al., 2015; Emsbo et al., 2015; Xing et al., 2021). For example, diagenetic uptake of REYs has been widely applied to explain REY enrichment in bioapatite and phosphorites (Kocsis et al., 2010; Chen et al., 2015; Francovschi et al., 2020), but in-situ analyses showed that diagenetic alteration mainly enriches REYs in apatite and phosphate nodule rims (Lumiste et al., 2019; Ye et al., 2021).

During the early Cambrian, widespread phosphorites occurred at shelf (mainly large-scale phosphorites) and near-slope (mainly small-scale phosphate concretions) settings on the Yangtze Block, South China (Steiner et al., 2007). However, only the outer-shelf (large-scale) Zhijin (ZJ) phosphorites and series near-slope (small-scale) phosphate concretions have been reported to have extraordinary REY enrichment (Chen et al., 2013; Zhu et al., 2014; Gao et al., 2018; Ye et al., 2021). Compared to the ZJ phosphorites, other coeval shelf (large-scale) phosphorites on the Yangtze Block contain much lower REYs (Chen et al., 2013; Ou, 2015; Xiao et al., 2018; Liu and Zhou, 2020). To understand the discrepant REY enrichment in phosphorites, the high-REY ZJ phosphorites and two comparative low-REY phosphorites (Meishucun-MSC and Xia'an-X'A phosphorites) on the Yangtze Block were studied with mineralogy, bulk-rock elements, total organic carbon (TOC), in-situ elements, and Zn-Fe isotopes. The three studied phosphorites were deposited almost simultaneously, which can greatly preclude the effects of secular variations in oceanic REY chemistry (Emsbo et al., 2015).

## 2. GEOLOGICAL SETTING

### 2.1. Paleogeography and lithostratigraphy

The South China Block comprises the Yangtze and Cathaysia Blocks (Li et al., 2008). During the early Cambrian, the Yangtze Block developed shelf, slope, and basin (called the Nanhua Basin) paleogeographic settings from northwest to southeast (Fig. 1). The lower Cambrian sedimentation was well-preserved on the Yangtze Block with systematic changes in sedimentary facies (Zhu et al., 2003; Steiner et al., 2007). The shelf setting mainly developed carbonates (e.g., Yanjiahe Formation), whereas the slope and basin settings were dominated by black shales (e.g., Niutitang Formation) and cherts (e.g., Liuchapo Formation) (Zhu et al., 2003; Feng et al., 2014; Zhang et al., 2020). In particular, widespread phosphorite deposition occurred at shelf and near-slope locations during the earliest Cambrian (Figs. 1 and 2). The large-scale (thickly bedded) phosphorites occurred mainly in inner-shelf settings, such as the Leibo (LB) and Mabian (MB) phosphorites in Sichuan and the MSC phosphorites in Yunnan (Fig. 1), in which ΣREY concentrations are typically moderate (~200–400 ppm) (Ou, 2015; Liu and Zhou, 2020). Additionally, thin-layer and concretionary phosphorites are more common at outer-shelf locations, but two large-scale phosphorites developed, namely, the ZJ and X'A phosphorites in Guizhou. Previous studies showed that the ZJ and X'A phosphorites yield extremely high ΣREY (~500–1500 ppm; Xing et al., 2021) and very low ΣREY concentrations (<200 ppm; Xiao et al., 2018), respectively. In contrast, the near-slope locations are dominated by small-scale concretionary phosphorites, in which ΣREY concentrations are comparable to those of the ZJ phosphorites (~500–1500 ppm; Chen et al., 2013, Gao et al., 2018; Ye et al., 2021). In this study, the large-scale MSC, ZJ, and X'A phosphorites in shelf settings with systematic differences in ΣREY concentrations were studied.

### 2.2. The studied phosphorites

The MSC phosphorites, located in Jinning County of Yunnan Province (Fig. 1), mainly occurred in the Zhongyicun Member of the Zhujiaqing Formation (Fig. 2). The Zhujiaqing Formation contains the Xiaowaitoushan Member at the bottom, the Zhongyicun Member in the middle, and the Dahai Member at the top. The Xiaowaitoushan Member and the Dahai Member are dominated by sandy dolostones (Wen et al., 2011; Liu and Zhou, 2017). The Zhujiaqing Formation was overlain by the Shiyantou Formation (mainly black shales) and underlain by the Denying Formation (mainly dolostones). The thickness of the MSC phosphorites is ~10 m; this phosphorite unit is separated by a volcanic tuff layer in the middle position (Fig. 2).

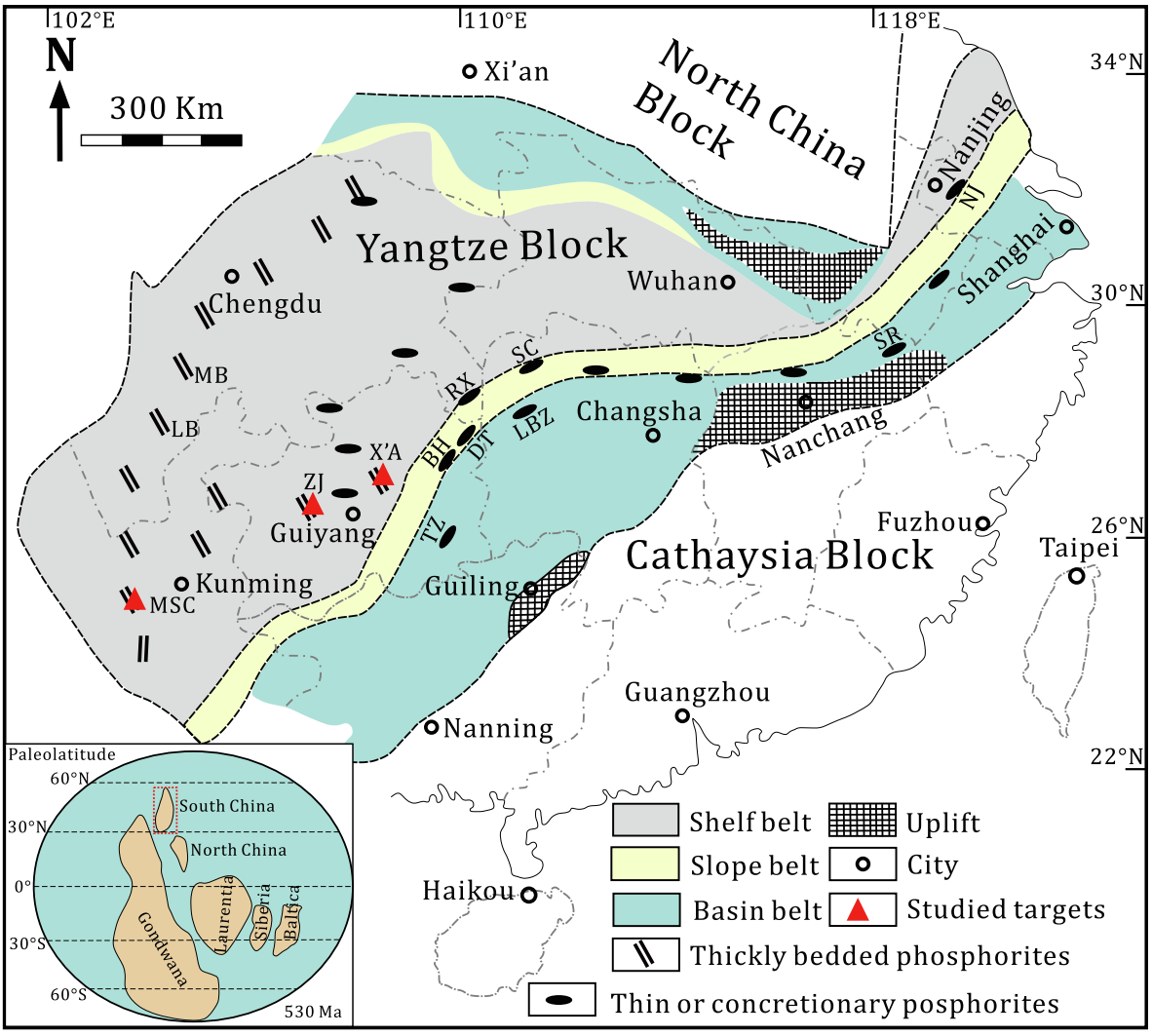


Fig. 1. Paleo-geographic map of South China during the early Cambrian, showing the locations of the studied and mentioned phosphorites or phosphate concretions in the main text (modified from Steiner et al., 2007). MSC-Meishucun (here), ZJ-Zhijin (here), X'A-Xia'an (here), LB-Leibo (Ou, 2015), MB-Mabian (Ou, 2015), DT-Daotuo (Ye et al., 2021), RX-Rongxi (Gao et al., 2018), LBZ-Longbizui (Zhu et al., 2014), SC-Sancha (Zhu et al., 2014), TZ-Tianzhu (Chen et al., 2013), BH-Bahuang (Chen et al., 2013), SR-Shangrao (Chen et al., 2013), NJ-Nanjing (Chen et al., 2013).

Phosphorites mainly occurred as massive, oolitic, and banded structures. Ripple marks can be observed at the boundaries between dolomitic layers and phosphatized layers, which may reflect that these phosphorites were deposited in a nearshore setting above the fair-weather wave base (Liu and Zhou, 2017, 2020). The first appearance of small shelly fossils was recorded in the basal Zhujiaqing Formation, which may approximate the Ediacaran-Cambrian (E-C) boundary (Sato et al., 2014). In chronostratigraphy, two tuff layers developed in the middle Zhongyicun Member and the basal Dahai Member, which yield zircon U-Pb ages of 535.2 ± 1.7 Ma and 523.9 ± 6.7 Ma, respectively (Fig. 2; Zhu et al., 2009; Okada et al., 2014).

The ZJ phosphorites, located in Zhijin County of Guizhou Province, mainly occurred in the Gezhongwu Formation (Figs. 1 and 2). The Gezhongwu Formation is underlain by the carbonates of the Dengying Formation and overlain by the black shales of the Niutitang Formation. The thickness of the ZJ phosphorites is ~20 m (Liu et al., 2020); the lower part is dominated by near-pure phosphorites ($P_2O_5$ > 15% and MgO < 10%), whereas the upper part is dominated by phosphatized dolostones ($P_2O_5$ < 15% and MgO > 10%). These phosphorites mainly occur as massive, lenticular, and banded structures (Liu and Zhou, 2020). Field observations found that oolitic textures and ripple marks are rarely developed in the ZJ phosphorites, indicating that these phosphorites were deposited in an offshore setting below the fair-weather wave base (Liu and Zhou, 2020). Similarly, the ZJ phosphorites were reported to have abundant small shelly fossils (Mao et al., 2013), which may indicate simultaneous phosphogenesis with the MSC phosphorites. Moreover, a Ni-Mo sulfide layer developed immediately above the phosphorites in the ZJ area, which yields Re-Os isochron ages of 521 ± 5 Ma

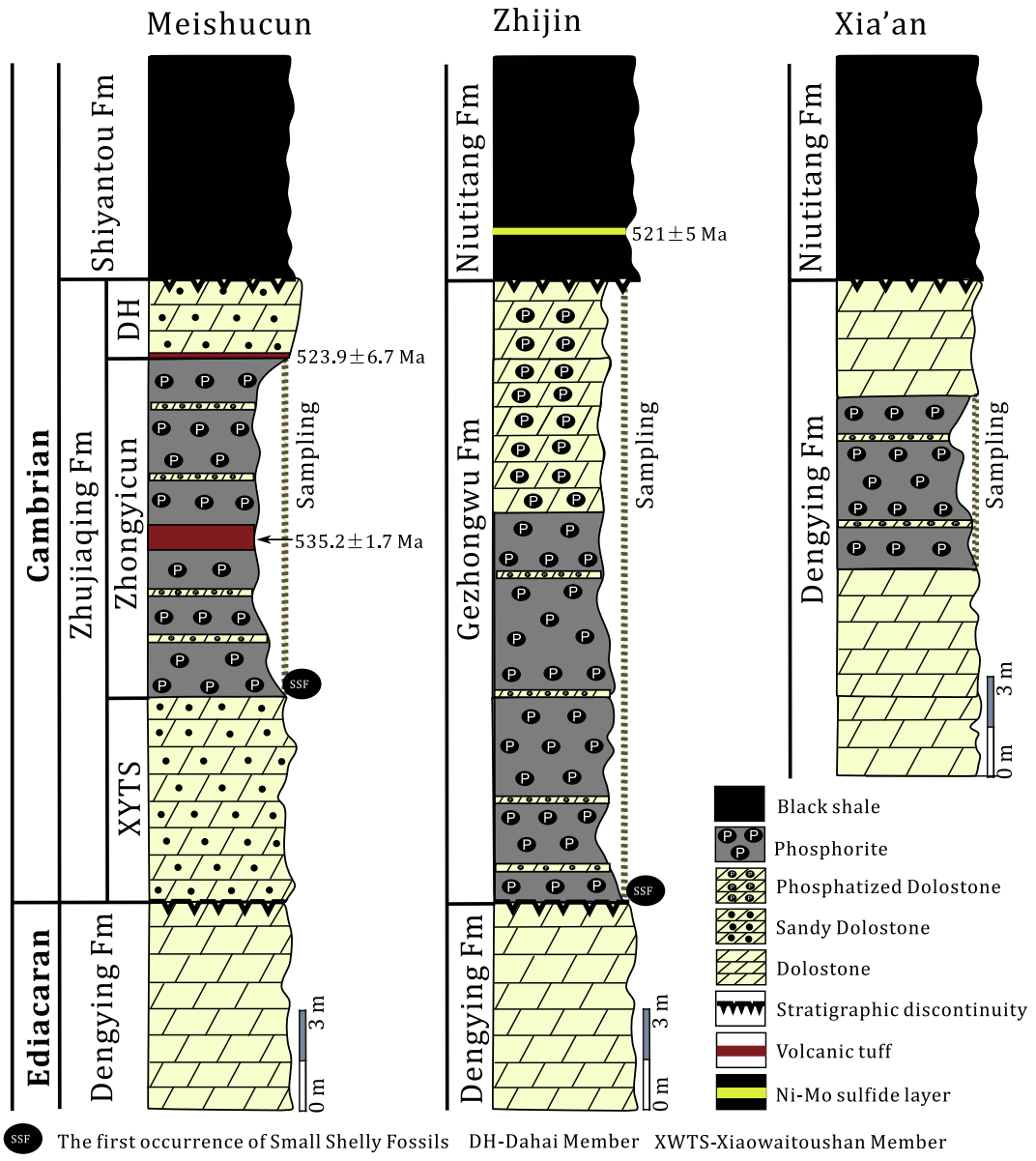


Fig. 2. The stratigraphic columns of the three studied phosphorite deposits on the Yangtze Block, South China (marked with sampling ranges). The chronostratigraphic information of the Meishucun and Zhijin phosphorite deposits was cited from Zhu et al. (2009), Xu et al. (2011) and Okada et al. (2014).

(Xu et al., 2011), comparable to the ages of tuff in the basal Dahai Member in the MSC section (523.9 ± 6.7 Ma; Okada et al., 2014).

The X'A phosphorites, located in Weng'an County of Guizhou Province, mainly occurred in the uppermost Dengying Formation (Fig. 2). The Dengying Formation is uncomfortably overlain by the black shales of the Niutitang Formation. Specifically, phosphorite beds developed ~4 m below the boundary of the Dengying and Niutitang formations (Fig. 2). The X'A phosphorites are ~5 m thick and interbedded with dolostones. Notably, the X'A phosphorites are characterized by phosphatized (columnar) stromatolites with alternating occurrences of apatite lamina in a lighter color and algal dolomite lamina in a darker color (Zhang, 2016). The formation of stromatolite phosphorites generally reflects authigenic phosphatization of microbial mats (Krajewski et al., 2000; Caird et al., 2017). Modern stromatolites mainly develop in subtidal environments (Reid et al., 1995), indicating that the X'A phosphorites may have been deposited in a similar subtidal environment (Zhang, 2016). No biostratigraphic marks or isotope ages are available in the X'A phosphorites. In lithostratigraphy, the MSC and ZJ phosphorites immediately overlie the Dengying Formation, whereas the X'A phosphorites occur in the uppermost Dengying Formation. Therefore, the X'A phosphorites appear to have been deposited slightly earlier than the MSC and ZJ phosphorites if the Denying Formation is synchronous. However, no other large-scale

phosphorites have been found in the top Dengying Formation on the Yangtze Block except the X'A phosphorites (Zhang, 2016). Therefore, the X'A phosphorites are likely to be isochronous products with the MSC and ZJ phosphorites, although this hypothesis needs further confirmation.

## 3. SAMPLES AND ANALYTICAL METHODS

### 3.1. Samples

Twenty-one near-pure phosphorites and five phosphatized dolostones in MSC, eighteen phosphorites and eighteen phosphatized dolostones in ZJ, and ten phosphorites and three phosphatized dolostones in X'A were sampled. The near-pure phosphorites were defined by $P_2O_5$ content of > 15% (Papineau, 2010), and the phosphatized dolostones were classified by $P_2O_5$ content of 1%–15% and MgO content of > 10%. In later discussion, we distinguish the phosphatized dolostones from near-pure phosphorites only in Section 5.4.2 (collectively referred to as phosphorites in other Sections). The MSC and X'A phosphorites were collected from fresh outcrops, whereas the ZJ samples were collected from a drill core (ZK-2603). Our sampling covers the entire phosphorite strata in the studied areas with a sampling span of ~0.5–1.0 m (Fig. 2). Samples used for geochemical analyses were firstly cut with a water-cooled cutting machine to remove stale surfaces and visible veins. Treated samples were then ground to 200-mesh powders, and all subsequent geochemical analyses were carried out on these powders. More than half of the analyzed samples were cut to make 50–100 μm thick sections for petrographic and mineralogical observation.

### 3.2. Methods

#### 3.2.1. Petrography and mineralogy

All thin sections were carefully examined under light microscopy and then coated with carbon and examined under high vacuum conditions in a JSM-7800F scanning electron microscope (SEM) at the Institute of Geochemistry, Chinese Academy of Sciences (IGCAS). The beam current was 10nA with an accelerating voltage of 20 kV to enhance chemical contrasts. The mineral composition in phosphorites was determined with an equipped TEAM Apollo XL energy-dispersive spectrometer (EDS).

#### 3.2.2. Bulk-rock major and trace elements and TOC

Analyses of major and trace elements were conducted using the ME-XRF26F and ME-MS61r methods, respectively, at ALS Chemex (Guangzhou) Co., Ltd. Powder samples of ~2 g were used for major element analysis. The major elements were determined by X-ray fluorescence (XRF) through lithium tetraborate powder pelleting. Powder samples of ~50 mg were used for trace element analysis. The powder samples were completely digested by a concentrated $HNO_3$ and HF mixture and then dissolved in 2% $HNO_3$ for ICP-MS measurement, before which a quantitative Rh internal standard solution was added to correct matrix effects and instrument drift. Five USGS standards (BHVO-2, BCR-2, COQ-1, NOD-A-1, and NOD-P-1) were analyzed together with our samples, which suggested that the relative errors were better than 5% for major elements and 3% for trace elements.

TOC analysis was accomplished at ALS Chemex (Guangzhou) Co., Ltd, following the method of C-IR17. Powder samples of ~3 g were treated several times with 6 N HCl to remove carbonates (inorganic carbon). The final solution was filtered, and solid residues were dried. The residues were then sent into an infrared induction furnace and combusted with near-pure $O_2$. The carbon dioxide produced by burning organic carbon was finally determined by a Leco (CS844) C-S analyzer. The relative errors for TOC analysis are better than 5% according to the analyses of two graphite standards, GGC-09 (2.80%) and GGC-08 (0.57%) (Geostats Pty. Ltd., Australia).

#### 3.2.3. In-situ elemental analyses

Apatite, Fe-oxide, and dolomite were analyzed with trace element concentrations by LA-ICP-MS (Agilent 7900 ICP-MS equipped with a GeoLasPro 193-nm ArF excimer laser) at the IGCAS. During spot analyses, the beam size was 22 μm, and the laser pulse energy was 65 mJ with a pulse frequency of 10 Hz. Each analysis comprised a 20 s background measurement (laser-off) followed by a 50 s data acquisition. To calibrate elemental content, multiple standards were analyzed before and after every ten samples (NIST610, NIST612, Durango, BC-28, GSE-1G, BCR-2G, BHVO-2G, BIR-1G, and MACS-3). Data calculation was performed by ICPMSDataCal software (Liu et al., 2008). The results of quality-control standards for apatite (Durango, USGS standard), Fe-oxide (BC-28, laboratory standard), and dolomite (MACS-3, USGS standard) suggest that relative analytical errors are lower than 10%. During elemental mapping, a beam size of 36 μm and a small line overlap (2 μm) were programmed to avoid line gaps. Element maps were compiled and processed using the program Iolite (Paton et al., 2011). The standard materials of NIST 610 and NIST 612 were analyzed immediately before and after sample analyses, which allowed quantitative elemental mapping.

#### 3.2.4. Bulk-rock Zn and Fe isotope analyses

All chemical procedures for Zn and Fe isotope analyses were conducted in an ultra-clean laboratory, during which purified acids and ultrapure water were used for sample digestion and elemental purification. Powder samples of ~100 mg were dissolved in 4 ml aqua regia at 120 ℃ for two days to ensure adequate extraction of Zn and Fe from phosphorites. The sample solution was evaporated and treated twice with 0.5 mL concentrated HCl to convert the cations to a chloride form. The final solution was evaporated to dryness and then dissolved in 1 mL 2 N HCl for Zn chemical purification and 6 N HCl for Fe chemical purification. Zn and Fe were purified through column chromatography using AGMP-1 anion exchange resin (100–200 mesh) according to the procedures reported by Tang et al. (2006). Zn was separated from other matrix elements through 2 N HCl wash, and then Zn was eluted with 0.5 N $HNO_3$. Fe was separated from other interfering

elements through 6 N HCl wash, and then Fe was eluted with 2 N HCl.

Zn and Fe isotopic ratios were measured using a Neptune MC-ICP-MS at the IGCAS. A standard-sample bracketing approach was applied to correct the instrumental mass discrimination. Zn isotopic compositions were measured relative to the IRMM 3702 standard and then reported relative to the JMC Lyon Zn standard based on the published difference between IRMM3702 Zn and JMC Lyon Zn ($\Delta^{66}Zn_{IRMM3702\text{-}JMC\ Lyon\ Zn} = 0.29‰$, Moeller et al., 2012). The Fe isotopic compositions were measured and reported relative to the IRMM-014 standard. The accuracy and reproducibility of Zn and Fe isotope analyses were evaluated by repeated analyses of standard materials, NOD-P-1 ($\delta^{66}Zn = 0.79 \pm 0.08‰$), NOD-A-1 ($\delta^{66}Zn = 0.94 \pm 0.04‰$), NIST SRM 683 ($\delta^{66}Zn = 0.15 \pm 0.04‰$), BHVO-2 ($\delta^{56}Fe = 0.11 \pm 0.05‰$), BCR-2 ($\delta^{56}Fe = 0.07 \pm 0.06‰$), and CAGS-Fe ($\delta^{56}Fe = 0.82 \pm 0.07‰$). The Zn and Fe isotopic compositions of the standard materials are consistent with previous publications (Zhao et al., 2012; Tang et al., 2016; Isson et al., 2018; Yang et al., 2018a).

*3.2.5. Elemental calculations*

REY concentrations were normalized to the Post-Archean Australian shales (Taylor and McLennan, 1985) and normalized concentrations are indicated by the subscript "N". The cerium anomaly (Ce/Ce*) was calculated using the conventional calculation equations: $Ce/Ce^* = 2*Ce_N/(La_N + Pr_N)$. The MREY anomaly (MREY/MREY*) was calculated as: $MREY/MREY^* = 2*(Sm_N + Eu_N + Gd_N + Tb_N + Dy_N)_{average}/[(La_N + Ce_N + Pr_N + Nd_N)_{average} + (Ho_N + Er_N + Tm_N + Yb_N + Lu_N)_{average}]$ (Zhang et al., 2016). The Pr/Pr* parameter was defined as: $Pr/Pr^* = 2Pr_N/(Ce_N + Nd_N)$ (Bau and Dulski, 1996).

## 4. RESULTS

### 4.1. Petrography and mineralogy

The major mineral components in the studied phosphorites are francolite (carbonate fluorapatite) and dolomite. Francolite tends to occur as aggregates (composed of numerous nano-scale francolites) in our phosphorites, granular or structureless. The apatite grains in the MSC phosphorites are mainly well-rounded or sub-rounded (Fig. 3A and B), in which francolites are tightly stacked and well-crystallized (Fig. 3C). Notably, small apatite grains coated with secondary phosphate growth (secondary phosphate deposition after reworking) are common in the MSC phosphorites (Fig. 3A; Wen et al., 2011). The apatite grains in the ZJ phosphorites are present either as sub-rounded or fossil-shaped and lack secondary phosphate growth (Fig. 3D and E), in which francolites are tightly stacked and well-crystallized, similar to the MSC francolites (Fig. 3F). Notably, abundant phosphatized small shelly fossils occurred in the ZJ phosphorites (Mao et al., 2013), especially in the ZJ near-pure phosphorites (Fig. 3D). The X'A phosphorites are characterized by phosphatized (columnar) stromatolites (Zhang, 2016), in which francolites are poorly crystallized with structureless aggregates (Fig. 3G–I and Supplementary Fig. S1). In addition, Fe-oxide is common in the studied phosphorites (Fig. 3B, E, and H), whereas Fe-sulfide (pyrite) was only observed in a few ZJ and X'A phosphorites in minor amounts (not shown).

### 4.2. Bulk-rock major and trace elements and TOC

The results of major and trace elements and TOC of bulk-rock are shown in Table 1 and Supplementary Table S1. The ΣREY content in the studied phosphorites changes widely. Extraordinary ΣREY enrichment occurs in the ZJ phosphorites (141–2041 ppm and 834 ppm on average), which is much higher than the ΣREY content of the MSC (104–441 ppm and 280 ppm on average) and X'A phosphorites (19–343 ppm and 92 ppm on average). Interestingly, ZJ near-pure phosphorites ($P_2O_5 > 15\%$) generally contain ΣREY at > 1000 ppm, whereas ZJ phosphatized dolostones ($P_2O_5 < 15\%$ and $MgO > 10\%$) generally produce ΣREY at < 500 ppm (Table 1), indicating that bulk-rock REYs are predominantly carried by phosphate mineral. Notably, REY-enriched ZJ phosphorites yield lower Y/Ho ratios (54 ± 2.5) and higher $Fe_2O_3$ content (0.99% ± 0.68) than low-REY MSC (Y/Ho ratios = 60 ± 5.0; $Fe_2O_3 = 0.45\% \pm 0.26$) and X'A phosphorites (Y/Ho ratios = 64 ± 4.5; $Fe_2O_3 = 0.21\% \pm 0.14$). The Ce/Ce* values are similar in the ZJ and MSC phosphorites (0.39 ± 0.03 and 0.33 ± 0.07, respectively), which are slightly lower than the Ce/Ce* values in the X'A phosphorites (0.54 ± 0.06). The ZJ and MSC phosphorites also yielded similar TOC content (0.22% ± 0.09 and 0.29% ± 0.26, respectively) (Liu and Zhou, 2020), which is slightly higher than that of the X'A phosphorites (0.08 % ± 0.04).

### 4.3. In-situ elemental analyses

The results of in-situ trace elements of apatite grains, Fe-oxide, and dolomite are shown in Supplementary Table S2. Similar to the bulk-rock chemistry composition, the average ΣREY content is highest in the ZJ apatite grains (1547 ppm), followed by the MSC apatite grains (327 ppm) and then by the X'A apatite grains (107 ppm). Our new in-situ results are consistent with previous studies, in which the average in-situ ΣREY content was 384 ppm in the MSC apatite grains (Liu and Zhou, 2020) and 1382 ppm (Liu et al., 2020), 1654 ppm (Lou et al., 2020), and 2471 ppm (Liu and Zhou, 2020) in the ZJ apatite grains. Relative to apatite grains, the ΣREY content in the Fe-oxide and dolomite of the studied phosphorites are much lower. The ΣREY are < 1–15 ppm in MSC, 10–20 ppm in ZJ, 13–48 ppm in X'A for Fe-oxide and 3–5 ppm in MSC, 56–139 ppm in ZJ, and < 1 ppm in X'A for dolomite. Notably, the ZJ dolomite also contains the highest ΣREY content compared to the MSC and X'A dolomite, similar to the ΣREY gradients in apatite grains. Additionally, REY mapping shows that the REY content of apatite grains is much higher than that of dolomite (Fig. 4), consistent with in-situ chemical analyses. Moreover, REY-enriched rims were observed in the MSC apatite

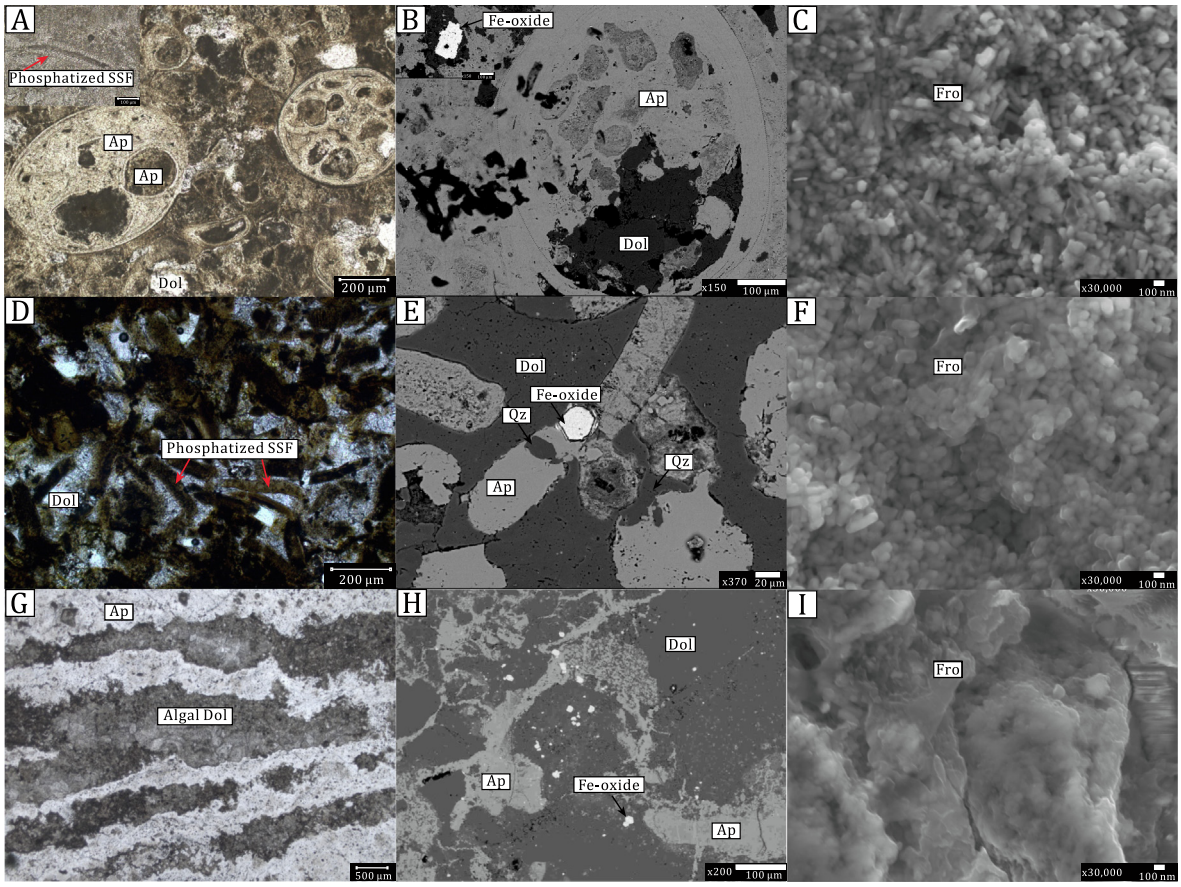


Fig. 3. Thin section photomicrographs and SEM images of the Meishucun (A, B, and C), Zhijin (D, E, and F), and Xia'an (G, H, and I) phosphorites, showing major mineral components and apatite textures. A, D and G are optical photomicrographs; B, E, and H are backscattered scanning electron microscope images; C, F, and I are secondary electron images. Abbreviations: Ap = apatite aggregates, Dol = dolomite, Fro = francolite, Qz = quartz, SSF = Small Shelly Fossils.

grains, whereas the REY distributions in the ZJ apatite grains and X'A structureless aggregates were homogeneous (Fig. 4). The homogeneous REY distributions in the ZJ apatite grains have also been confirmed through electron probe microanalysis (EPMA) mapping by Liu et al. (2020).

### 4.4. Bulk-rock Zn and Fe isotopes

The Zn and Fe isotope results of the studied phosphorites are shown in Table 1. The ZJ and X'A phosphorites yield similarly low $\delta^{66}Zn$ values, which are 0.16‰ and 0.14‰ on average, respectively. In contrast, the MSC phosphorites yield much higher $\delta^{66}Zn$ values ($\delta^{66}Zn_{average} = 0.75‰$), similar to those of Ediacaran phosphorites in South China (Fan et al., 2018). The $\delta^{56}Fe$ values in the X'A phosphorites are relatively homogeneous (~0.0‰), similar to the $\delta^{56}Fe$ values of the MSC phosphorites (Fan et al., 2016). In contrast, the ZJ phosphorites give widely changing $\delta^{56}Fe$ values from −0.54‰ to 0.45‰. Generally, near-pure phosphorites produce positive $\delta^{56}Fe$ values (~0.0–0.45‰), whereas phosphatized dolostones yield negative $\delta^{56}Fe$ values.

## 5. DISCUSSION

### 5.1. REY sources and post-depositional alteration

Sedimentary phosphorites have two potential REY sources, lithogenous and hydrogenous (Zhang et al., 2016; Francovschi et al., 2020). If marine sediments contain substantial terrigenous detritus, REY signals are likely to be dominated by lithogenous REYs. The admixture of terrigenous detritus can be detected by the correlations between bulk-rock ΣREY and $Al_2O_3$ content. In the studied phosphorites, $Al_2O_3$ content is commonly low (mostly < 1%) and shows no obvious correlations with ΣREY (Fig. 5A), indicating negligible detrital admixture. In addition, lithogenous REYs are generally characterized by chondritic Y/Ho ratios (~25–30; Pack et al., 2007). However, all of the studied phosphorites show seawater-like Y/Ho ratios (~50–70; Fig. 5B), indicating that phosphorite REYs were mainly sourced from seawater rather than continental detritus.

Also, REY chemistry in seawater is likely to be altered during paleo-climate changes, which can result in different REY enrichment in phosphorites deposited at different

Table 1
Major elements (%), trace element Zn (ppm), REY parameters, TOC, and Zn and Fe isotopes in the studied phosphorites.

| Sample | Lithology | $P_2O_5$ | CaO | MgO | $Al_2O_3$ | $Fe_2O_3$ | $SiO_2$ | $SO_3$ | Zn | ΣREY | Y/Ho | Ce/Ce* | $La_N/Sm_N$ | $La_N/Yb_N$ | M/M* | TOC | $\delta^{66}Zn$ | 2SD | $\delta^{56}Fe$ | 2SD | Fe/Al |
|---|---|---|---|---|---|---|---|---|---|---|---|---|---|---|---|---|---|---|---|---|---|
| Meishucun phosphorites | | | | | | | | | | | | | | | | | | | | | |
| ZYC-27 | Phosphatized Dol. | 4.60 | 23.84 | 12.28 | 2.96 | 1.31 | 24.95 | 0.08 | 27.3 | 104 | 48 | 0.68 | 0.86 | 0.57 | 1.02 | - | - | - | 0.11 | 0.15 | 0.58 |
| ZYC-26 | Near-pure Phos. | 21.05 | 42.28 | 9.27 | 0.42 | 0.55 | 4.38 | 0.28 | 15.3 | 257 | 67 | 0.45 | 1.17 | 1.20 | 1.21 | - | 0.72 | 0.02 | −0.16 | 0.04 | 1.73 |
| ZYC-25 | Phosphatized Dol. | 10.28 | 35.11 | 14.69 | 0.35 | 0.60 | 4.93 | 0.25 | 6.5 | 166 | 62 | 0.34 | 1.13 | 0.87 | 1.10 | - | - | - | - | - | 2.26 |
| ZYC-24 | Phosphatized Dol. | 12.28 | 36.70 | 13.86 | 0.31 | 0.56 | 3.79 | 0.16 | 6.9 | 205 | 66 | 0.32 | 1.22 | 1.01 | 1.14 | - | - | - | −0.21 | 0.02 | 2.39 |
| ZYC-23 | Phosphatized Dol. | 8.75 | 34.19 | 15.48 | 0.60 | 1.19 | 4.10 | 0.09 | 10.2 | 146 | 61 | 0.34 | 1.12 | 0.75 | 1.08 | - | - | - | - | - | 2.62 |
| ZYC-22 | Near-pure Phos. | 27.76 | 45.97 | 5.83 | 0.34 | 0.43 | 4.11 | 0.33 | 5.4 | 343 | 70 | 0.41 | 1.32 | 1.36 | 1.17 | - | - | - | 0.07 | 0.10 | 1.67 |
| ZYC-21 | Near-pure Phos. | 32.54 | 48.55 | 3.79 | 0.19 | 0.29 | 3.19 | 0.40 | 5.3 | 441 | 66 | 0.35 | 1.32 | 1.42 | 1.17 | - | 0.75 | 0.08 | −0.03 | 0.06 | 2.02 |
| ZYC-20 | Near-pure Phos. | 16.02 | 38.54 | 11.60 | 0.33 | 0.66 | 4.01 | 0.20 | 4.2 | 258 | 66 | 0.32 | 1.27 | 1.08 | 1.17 | - | - | - | - | - | 2.64 |
| ZYC-19 | Near-pure Phos. | 17.25 | 38.83 | 9.81 | 1.21 | 0.50 | 6.46 | 0.21 | 7.0 | 304 | 61 | 0.35 | 1.26 | 0.89 | 1.09 | - | - | - | 0.03 | 0.06 | 0.55 |
| ZYC-18 | Phosphatized Dol. | 10.13 | 34.70 | 15.39 | 0.44 | 0.72 | 2.27 | 0.15 | 5.2 | 156 | 58 | 0.32 | 1.15 | 0.78 | 1.11 | - | 1.36 | 0.10 | - | - | 2.16 |
| ZYC-17 | Near-pure Phos. | 30.02 | 46.37 | 3.48 | 0.43 | 0.39 | 8.21 | 0.30 | 3.1 | 259 | 62 | 0.35 | 1.39 | 1.14 | 1.10 | - | - | - | −0.06 | 0.20 | 1.20 |
| ZYC-15 | Near-pure Phos. | 18.71 | 27.26 | 0.11 | 0.11 | 0.29 | 49.96 | 0.03 | 21.2 | 271 | 48 | 0.66 | 0.77 | 1.65 | 1.46 | - | 0.50 | 0.06 | 0.43 | 0.16 | 3.48 |
| ZYC-14 | Near-pure Phos. | 35.44 | 50.81 | 1.88 | 0.15 | 0.32 | 3.29 | 0.17 | 15.9 | 256 | 59 | 0.46 | 1.29 | 1.53 | 1.23 | - | - | - | −0.02 | 0.13 | 2.82 |
| ZYC-13 | Near-pure Phos. | 36.26 | 51.67 | 1.68 | 0.16 | 0.20 | 2.04 | 0.22 | 15.7 | 297 | 61 | 0.41 | 1.58 | 1.73 | 1.18 | - | - | - | 0.02 | 0.09 | 1.65 |
| ZYC-12 | Near-pure Phos. | 36.12 | 51.35 | 1.65 | 0.14 | 0.25 | 2.35 | 0.07 | 19.6 | 287 | 63 | 0.38 | 1.55 | 1.72 | 1.21 | - | 0.61 | 0.07 | - | - | 2.36 |
| ZYC-11 | Near-pure Phos. | 35.48 | 50.94 | 1.92 | 0.15 | 0.38 | 2.45 | 0.09 | 9.3 | 308 | 64 | 0.36 | 1.43 | 1.65 | 1.23 | - | - | - | −0.05 | 0.11 | 3.35 |
| ZYC-10 | Near-pure Phos. | 33.85 | 49.98 | 2.79 | 0.13 | 0.38 | 2.50 | 0.02 | 10.0 | 339 | 60 | 0.35 | 1.26 | 1.50 | 1.32 | - | - | - | - | - | 3.86 |
| ZYC-09 | Near-pure Phos. | 36.22 | 50.99 | 1.41 | 0.18 | 0.28 | 4.08 | 0.68 | 16.8 | 400 | 59 | 0.34 | 1.19 | 1.49 | 1.35 | - | 0.70 | 0.05 | - | - | 2.05 |
| ZYC-08 | Near-pure Phos. | 23.80 | 41.31 | 6.11 | 0.42 | 0.31 | 11.32 | 0.38 | 23.4 | 278 | 55 | 0.37 | 0.92 | 1.41 | 1.48 | - | - | - | −0.05 | 0.11 | 0.97 |
| ZYC-07 | Near-pure Phos. | 23.23 | 41.28 | 6.63 | 0.35 | 0.32 | 10.11 | 0.43 | 4.7 | 317 | 55 | 0.37 | 0.95 | 1.40 | 1.43 | - | - | - | −0.06 | 0.09 | 1.21 |
| ZYC-06 | Near-pure Phos. | 29.23 | 44.48 | 3.46 | 0.36 | 0.32 | 11.31 | 0.48 | 4.8 | 438 | 52 | 0.38 | 0.88 | 1.45 | 1.46 | - | - | - | - | - | 1.17 |
| ZYC-05 | Near-pure Phos. | 31.62 | 47.00 | 2.60 | 0.29 | 0.43 | 9.04 | 0.55 | 3.4 | 423 | 55 | 0.35 | 0.95 | 1.52 | 1.48 | - | - | - | - | - | 1.96 |
| ZYC-04 | Near-pure Phos. | 32.38 | 48.02 | 2.94 | 0.26 | 0.33 | 5.62 | 0.58 | 9.0 | 326 | 58 | 0.36 | 1.03 | 1.55 | 1.45 | - | 0.77 | 0.08 | 0.03 | 0.01 | 1.68 |
| ZYC-03 | Near-pure Phos. | 21.38 | 41.94 | 8.89 | 0.27 | 0.33 | 4.77 | 0.33 | 8.1 | 184 | 58 | 0.36 | 1.10 | 1.54 | 1.34 | - | - | - | - | - | 1.61 |
| ZYC-02 | Near-pure Phos. | 33.51 | 49.49 | 2.85 | 0.16 | 0.16 | 4.56 | 0.28 | 15.0 | 218 | 60 | 0.38 | 1.33 | 1.79 | 1.27 | - | - | - | −0.16 | 0.07 | 1.32 |
| ZYC-01 | Near-pure Phos. | 36.22 | 52.08 | 1.88 | 0.21 | 0.20 | 2.18 | 0.48 | 38.2 | 295 | 56 | 0.44 | 1.20 | 1.88 | 1.37 | - | 0.71 | 0.02 | 0.03 | 0.10 | 1.26 |
| Zhijin phosphorites | | | | | | | | | | | | | | | | | | | | | |
| 2603–173 | Phosphatized Dol. | 3.94 | 28.10 | 15.45 | 0.33 | 1.29 | 14.90 | <0.01 | 18.0 | 280 | 53 | 0.38 | 0.99 | 1.11 | 1.31 | 0.17 | - | - | −0.49 | 0.03 | 5.16 |
| 2603–173.5 | Phosphatized Dol. | 2.57 | 26.90 | 15.00 | 0.61 | 0.65 | 17.41 | 0.06 | 36.0 | 205 | 52 | 0.39 | 0.97 | 1.11 | 1.31 | 0.38 | - | - | −0.11 | 0.01 | 1.41 |
| 2603–174 | Phosphatized Dol. | 1.75 | 25.90 | 16.15 | 0.81 | 1.09 | 16.86 | <0.01 | 40.0 | 180 | 51 | 0.39 | 0.96 | 0.83 | 1.17 | 0.19 | 0.23 | 0.02 | −0.27 | 0.03 | 1.78 |
| 2603–174.5 | Phosphatized Dol. | 7.46 | 31.30 | 14.70 | 1.85 | 0.91 | 9.20 | 1.28 | 36.0 | 381 | 50 | 0.43 | 0.98 | 1.32 | 1.36 | 0.29 | - | - | 0.10 | 0.03 | 0.65 |
| 2603–175 | Phosphatized Dol. | 2.68 | 27.10 | 16.15 | 0.56 | 0.99 | 15.70 | <0.01 | 21.0 | 220 | 52 | 0.39 | 0.95 | 0.89 | 1.23 | 0.14 | - | - | −0.23 | 0.03 | 2.33 |
| 2603–175.5 | Phosphatized Dol. | 6.77 | 29.10 | 13.55 | 0.46 | 0.90 | 17.42 | 0.01 | 153.0 | 504 | 51 | 0.38 | 0.88 | 1.41 | 1.46 | 0.30 | 0.19 | 0.05 | −0.14 | 0.01 | 2.58 |
| 2603–176 | Phosphatized Dol. | 2.03 | 27.10 | 16.05 | 0.40 | 0.46 | 15.92 | 0.08 | 54.0 | 141 | 54 | 0.38 | 1.15 | 0.98 | 1.13 | 0.19 | 0.36 | 0.02 | −0.04 | 0.04 | 1.52 |
| 2603–177 | Phosphatized Dol. | 4.06 | 26.40 | 14.50 | 0.69 | 0.61 | 20.31 | <0.01 | 77.0 | 250 | 53 | 0.38 | 1.09 | 1.22 | 1.28 | 0.17 | 0.35 | 0.06 | 0.08 | 0.00 | 1.17 |
| 2603–178 | Phosphatized Dol. | 2.75 | 26.10 | 15.10 | 1.23 | 1.97 | 16.92 | <0.01 | 8.0 | 193 | 54 | 0.39 | 1.06 | 1.07 | 1.24 | 0.20 | - | - | −0.30 | 0.05 | 2.12 |
| 2603–178.5 | Phosphatized Dol. | 4.10 | 26.80 | 14.25 | 0.40 | 2.10 | 17.79 | <0.01 | 8.0 | 237 | 56 | 0.39 | 1.07 | 1.22 | 1.28 | 0.23 | - | - | −0.37 | 0.02 | 6.93 |
| 2603–179 | Phosphatized Dol. | 2.92 | 25.90 | 14.70 | 1.36 | 2.05 | 18.20 | <0.01 | 8.0 | 201 | 55 | 0.38 | 1.04 | 1.10 | 1.23 | 0.18 | 0.19 | 0.01 | −0.32 | 0.00 | 1.99 |
| 2603–179.5 | Phosphatized Dol. | 3.51 | 26.00 | 14.50 | 1.17 | 3.97 | 16.78 | <0.01 | 7.0 | 215 | 56 | 0.38 | 1.09 | 1.16 | 1.21 | 0.39 | - | - | −0.39 | 0.05 | 4.48 |
| 2603–180 | Phosphatized Dol. | 4.16 | 28.60 | 15.05 | 0.50 | 1.21 | 14.88 | <0.01 | 31.0 | 293 | 58 | 0.37 | 1.16 | 1.46 | 1.29 | 0.16 | 0.05 | 0.01 | −0.09 | 0.02 | 3.20 |
| 2603–180.5 | Phosphatized Dol. | 5.05 | 28.80 | 14.35 | 0.46 | 1.20 | 15.80 | <0.01 | 32.0 | 310 | 60 | 0.37 | 1.18 | 1.47 | 1.31 | 0.17 | 0.10 | 0.00 | −0.07 | 0.07 | 3.45 |
| 2603–180.7 | Near-pure Phos. | 30.10 | 48.00 | 4.20 | 0.34 | 0.62 | 2.51 | 0.13 | 150.0 | 1364 | 53 | 0.34 | 0.95 | 1.70 | 1.46 | 0.22 | - | - | 0.20 | 0.04 | 2.41 |

| | | | | | | | | | | | | | | | | | | | | | |
|---|---|---|---|---|---|---|---|---|---|---|---|---|---|---|---|---|---|---|---|---|---|
| 2603–181.5 | Phosphatized Dol. | 11.30 | 36.30 | 14.35 | 0.19 | 0.55 | 3.60 | 0.03 | 102.0 | 535 | 56 | 0.32 | 1.00 | 1.52 | 1.38 | 0.22 | - | - | −0.33 | 0.07 | 3.82 |
| 2603–182 | Near-pure Phos. | 18.05 | 40.90 | 10.90 | 0.33 | 0.64 | 1.59 | 0.06 | 91.0 | 832 | 54 | 0.33 | 0.98 | 1.47 | 1.43 | 0.18 | - | - | 0.01 | 0.06 | 2.56 |
| 2603–182.5 | Near-pure Phos. | 36.70 | 51.70 | 0.39 | 0.81 | 0.90 | 3.18 | 0.23 | 280.0 | 2041 | 52 | 0.35 | 0.93 | 1.76 | 1.44 | 0.28 | - | - | 0.35 | 0.03 | 1.47 |
| 2603–183 | Near-pure Phos. | 16.35 | 39.70 | 11.90 | 0.20 | 0.88 | 2.43 | 0.06 | 128.0 | 765 | 54 | 0.33 | 0.97 | 1.55 | 1.50 | 0.19 | - | - | 0.02 | 0.01 | 5.81 |
| 2603–183.5 | Near-pure Phos. | 32.40 | 49.70 | 3.09 | 0.33 | 0.80 | 1.51 | 0.15 | 146.0 | 1465 | 53 | 0.33 | 1.01 | 1.61 | 1.43 | 0.20 | - | - | 0.31 | 0.06 | 3.20 |
| 2603–184 | Near-pure Phos. | 35.70 | 52.00 | 1.56 | 0.27 | 0.79 | 1.46 | 0.17 | 90.0 | 1812 | 53 | 0.33 | 1.01 | 1.73 | 1.47 | 0.19 | - | - | 0.27 | 0.06 | 3.86 |
| 2603–184.5 | Near-pure Phos. | 35.00 | 51.70 | 2.01 | 0.20 | 0.80 | 1.24 | 0.18 | 72.0 | 1721 | 56 | 0.34 | 1.06 | 1.80 | 1.44 | 0.19 | - | - | 0.30 | 0.02 | 5.28 |
| 2603–185 | Near-pure Phos. | 33.80 | 50.70 | 2.10 | 0.39 | 0.81 | 1.63 | 0.28 | 183.0 | 1405 | 57 | 0.34 | 1.09 | 1.69 | 1.40 | 0.18 | - | - | 0.31 | 0.02 | 2.74 |
| 2603–185.5 | Near-pure Phos. | 36.60 | 52.30 | 0.87 | 0.22 | 0.70 | 1.45 | 0.18 | 56.0 | 1730 | 58 | 0.34 | 1.09 | 1.77 | 1.43 | 0.22 | - | - | 0.31 | 0.01 | 4.20 |
| 2603–186 | Near-pure Phos. | 20.70 | 37.10 | 6.12 | 2.11 | 2.01 | 13.94 | 3.48 | 57.0 | 990 | 49 | 0.44 | 0.96 | 1.52 | 1.43 | 0.64 | - | - | 0.12 | 0.04 | 1.26 |
| 2603–186.5 | Phosphatized Dol. | 11.40 | 36.40 | 14.35 | 0.20 | 0.56 | 3.70 | 0.03 | 84.0 | 515 | 55 | 0.34 | 1.03 | 1.57 | 1.38 | 0.25 | - | - | −0.46 | 0.06 | 3.70 |
| 2603–187 | Near-pure Phos. | 37.70 | 54.00 | 0.39 | 0.16 | 0.53 | 0.78 | 0.24 | 197.0 | 1818 | 58 | 0.34 | 1.05 | 1.80 | 1.41 | 0.21 | - | - | 0.24 | 0.04 | 4.38 |
| 2603–187.5 | Near-pure Phos. | 36.40 | 52.90 | 0.69 | 0.20 | 0.68 | 1.21 | 0.19 | 151.0 | 1752 | 56 | 0.36 | 1.00 | 1.69 | 1.45 | 0.21 | - | - | 0.24 | 0.05 | 4.49 |
| 2603–188 | Phosphatized Dol. | 9.24 | 35.40 | 15.70 | 0.16 | 0.50 | 2.58 | 0.04 | 70.0 | 445 | 52 | 0.34 | 1.05 | 1.44 | 1.38 | 0.22 | - | - | −0.54 | 0.00 | 4.13 |
| 2603–189 | Phosphatized Dol. | 9.32 | 35.10 | 15.40 | 0.14 | 0.52 | 3.68 | 0.05 | 68.0 | 445 | 54 | 0.34 | 1.06 | 1.45 | 1.36 | 0.20 | −0.05 | 0.01 | −0.54 | 0.06 | 4.91 |
| 2603–189.5 | Near-pure Phos. | 35.70 | 51.90 | 1.38 | 0.28 | 0.62 | 2.24 | 0.24 | 160.0 | 1367 | 57 | 0.33 | 1.08 | 1.63 | 1.38 | 0.18 | - | - | 0.30 | 0.06 | 2.92 |
| 2603–190 | Near-pure Phos. | 17.95 | 40.30 | 10.85 | 0.53 | 0.72 | 2.77 | 0.12 | 102.0 | 780 | 55 | 0.34 | 1.01 | 1.51 | 1.42 | 0.21 | −0.01 | 0.01 | −0.06 | 0.02 | 1.79 |
| 2603–191 | Near-pure Phos. | 20.50 | 41.90 | 9.24 | 0.29 | 0.67 | 3.78 | 0.12 | 122.0 | 857 | 56 | 0.34 | 1.01 | 1.66 | 1.43 | 0.15 | 0.33 | 0.03 | −0.01 | 0.03 | 3.05 |
| 2603–192 | Near-pure Phos. | 33.10 | 50.30 | 2.77 | 0.46 | 0.74 | 1.93 | 0.23 | 54.0 | 1260 | 57 | 0.33 | 1.08 | 1.63 | 1.38 | 0.19 | 0.23 | 0.04 | 0.43 | 0.02 | 2.12 |
| 2603–193 | Near-pure Phos. | 33.40 | 50.30 | 2.57 | 0.33 | 0.68 | 2.35 | 0.23 | 78.0 | 1261 | 56 | 0.33 | 1.08 | 1.63 | 1.38 | 0.17 | 0.13 | 0.00 | 0.45 | 0.06 | 2.72 |
| 2603–193.9 | Near-pure Phos. | 34.30 | 51.20 | 2.31 | 0.25 | 0.66 | 1.86 | 0.23 | 132.0 | 1260 | 55 | 0.33 | 1.09 | 1.58 | 1.37 | 0.21 | 0.02 | 0.02 | 0.36 | 0.02 | 3.49 |
| Xia'an phosphorites | | | | | | | | | | | | | | | | | | | | | |
| 1132–12 | Near-pure Phos. | 29.72 | 47.52 | 4.58 | 1.19 | 0.56 | 2.28 | 0.80 | 401.0 | 343 | 54 | 0.50 | 1.01 | 0.70 | 1.11 | - | 0.37 | 0.11 | −0.08 | 0.09 | 0.62 |
| 1132–11 | Near-pure Phos. | 23.41 | 44.75 | 8.56 | 0.40 | 0.33 | 0.84 | 0.30 | 169.0 | 199 | 58 | 0.51 | 0.78 | 0.53 | 1.27 | - | 0.17 | 0.01 | −0.09 | 0.10 | 1.09 |
| 1132–10 | Near-pure Phos. | 22.35 | 44.99 | 8.82 | 0.03 | 0.22 | 0.09 | 0.53 | 182.0 | 81 | 59 | 0.49 | 0.79 | 0.39 | 1.04 | - | 0.19 | 0.05 | 0.02 | 0.10 | 9.69 |
| 1132–09 | Near-pure Phos. | 26.01 | 46.78 | 7.58 | 0.03 | 0.32 | 0.16 | 0.30 | 210.0 | 52 | 64 | 0.48 | 0.98 | 0.53 | 1.04 | - | 0.05 | 0.00 | - | - | 14.09 |
| 1132–08 | Near-pure Phos. | 24.41 | 45.66 | 8.46 | 0.02 | 0.07 | 0.08 | 0.28 | 101.0 | 52 | 67 | 0.46 | 1.08 | 0.55 | 1.00 | - | 0.07 | 0.03 | 0.00 | 0.09 | 4.62 |
| 1132–7.5 | Near-pure Phos. | 31.27 | 49.81 | 5.05 | 0.02 | 0.13 | 0.14 | 0.35 | 99.0 | 38 | 70 | 0.49 | 1.02 | 0.42 | 0.95 | - | 0.09 | 0.05 | 0.11 | 0.09 | 8.58 |
| 1132–07 | Phosphatized Dol. | 8.30 | 36.33 | 16.85 | 0.03 | 0.15 | 0.15 | 0.10 | 29.0 | 21 | 63 | 0.53 | 0.75 | 0.29 | 0.97 | - | −0.05 | 0.05 | - | - | 6.60 |
| 1132–6.5 | Phosphatized Dol. | 12.13 | 38.61 | 14.71 | 0.03 | 0.15 | 0.09 | 0.15 | 30.0 | 27 | 67 | 0.54 | 0.73 | 0.33 | 1.06 | - | 0.16 | 0.02 | - | - | 6.60 |
| 1132–06 | Phosphatized Dol. | 14.42 | 40.04 | 13.68 | 0.03 | 0.15 | 0.11 | 0.18 | 33.0 | 19 | 68 | 0.57 | 0.73 | 0.26 | 0.91 | - | 0.15 | 0.01 | - | - | 6.60 |
| 1132–5.5 | Near-pure Phos. | 26.87 | 47.21 | 7.34 | 0.03 | 0.09 | 0.11 | 0.33 | 46.0 | 35 | 65 | 0.58 | 0.64 | 0.29 | 1.03 | - | 0.15 | 0.03 | - | - | 3.96 |
| 1132–05 | Near-pure Phos. | 33.87 | 50.87 | 3.74 | 0.02 | 0.08 | 0.10 | 0.38 | 166.0 | 74 | 60 | 0.58 | 0.66 | 0.26 | 0.97 | - | 0.21 | 0.04 | - | - | 5.28 |
| 1132–04 | Near-pure Phos. | 22.13 | 44.38 | 9.59 | 0.02 | 0.25 | 0.05 | 0.28 | 220.0 | 108 | 64 | 0.63 | 0.62 | 0.26 | 0.98 | - | 0.05 | 0.01 | - | - | 16.51 |
| 1132–03 | Near-pure Phos. | 23.55 | 44.93 | 8.75 | 0.03 | 0.19 | 0.09 | 0.28 | 289.0 | 142 | 68 | 0.64 | 0.68 | 0.28 | 0.99 | - | 0.18 | 0.01 | - | - | 8.36 |

Partial major elements and all Fe isotopes of the Meishucun phosphorites (Fe-oxide fraction) were cited from Fan et al. (2016). Partial major elements and REYs and all Fe isotopes of the Xia'an phosphorites were cited from Xiao et al. (2018). "-" mean not measured, M/M* = MREY/MREY*, Phos. = Phosphorites, Dol. = Dolostone.

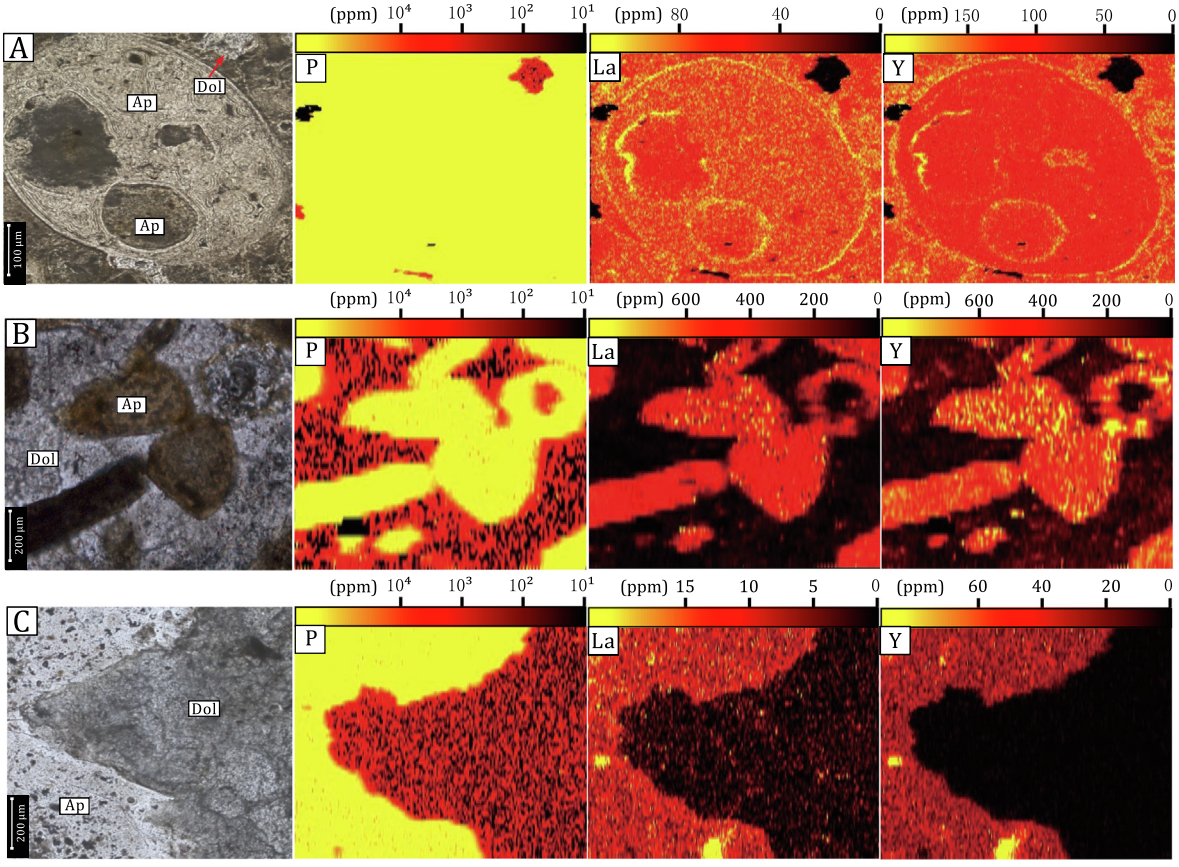


Fig. 4. Thin section photomicrograph and corresponding LA-ICP-MS mapping of REYs (represented by La and Y) in the Meishucun (A), Zhijin (B), and Xia'an (C) phosphorites. Scales of LA-ICP-MS images are expressed in ppm. Note that the Meishucun apatite grains developed REY-enriched rims. Abbreviations: Ap = apatite aggregates, Dol = dolomite.

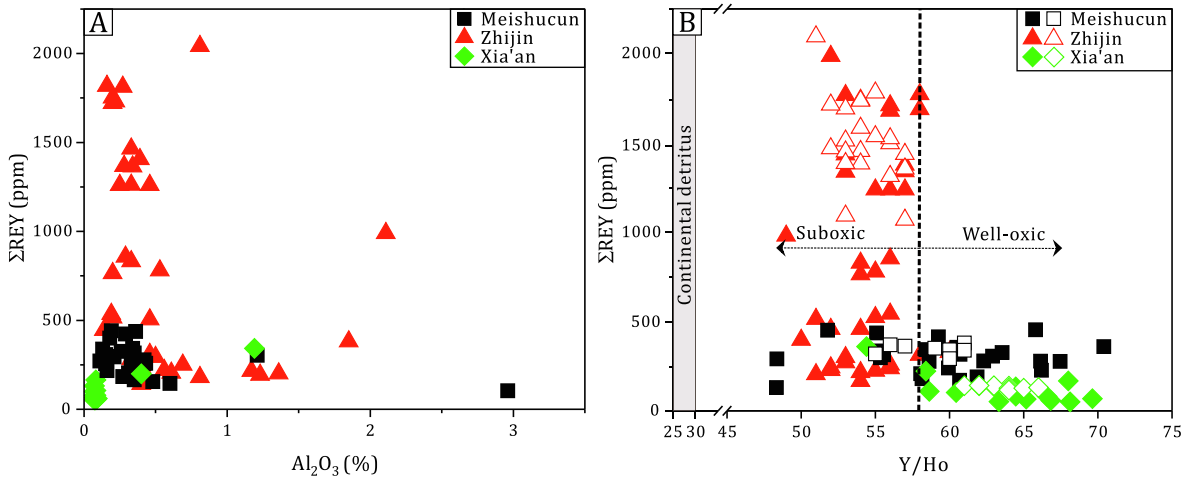


Fig. 5. ΣREY plotted against $Al_2O_3$ contents (A) and Y/Ho ratios (B) of the studied phosphorites. The poor correlations reflect insignificant detrital REY contributions. The slightly lower Y/Ho ratios in the ZJ phosphorites may suggest a suboxic deposition environment rather than detrital effects. The solid symbol represents bulk-rock data and the open symbol represents in-situ apatite data.

geological times (Banerjee et al., 2020; Buccione et al., 2021). As mentioned earlier, the MSC and ZJ phosphorites are isochronous products, but the X'A phosphorites are likely to be deposited slightly earlier than the MSC and ZJ phosphorites (Fig. 2). Notably, the MSC and ZJ phosphorites show similar MREY-enriched patterns, whereas the REY pattern in the X'A phosphorites is modern seawater-like (Fig. 6), indicating possible changes in seawa-

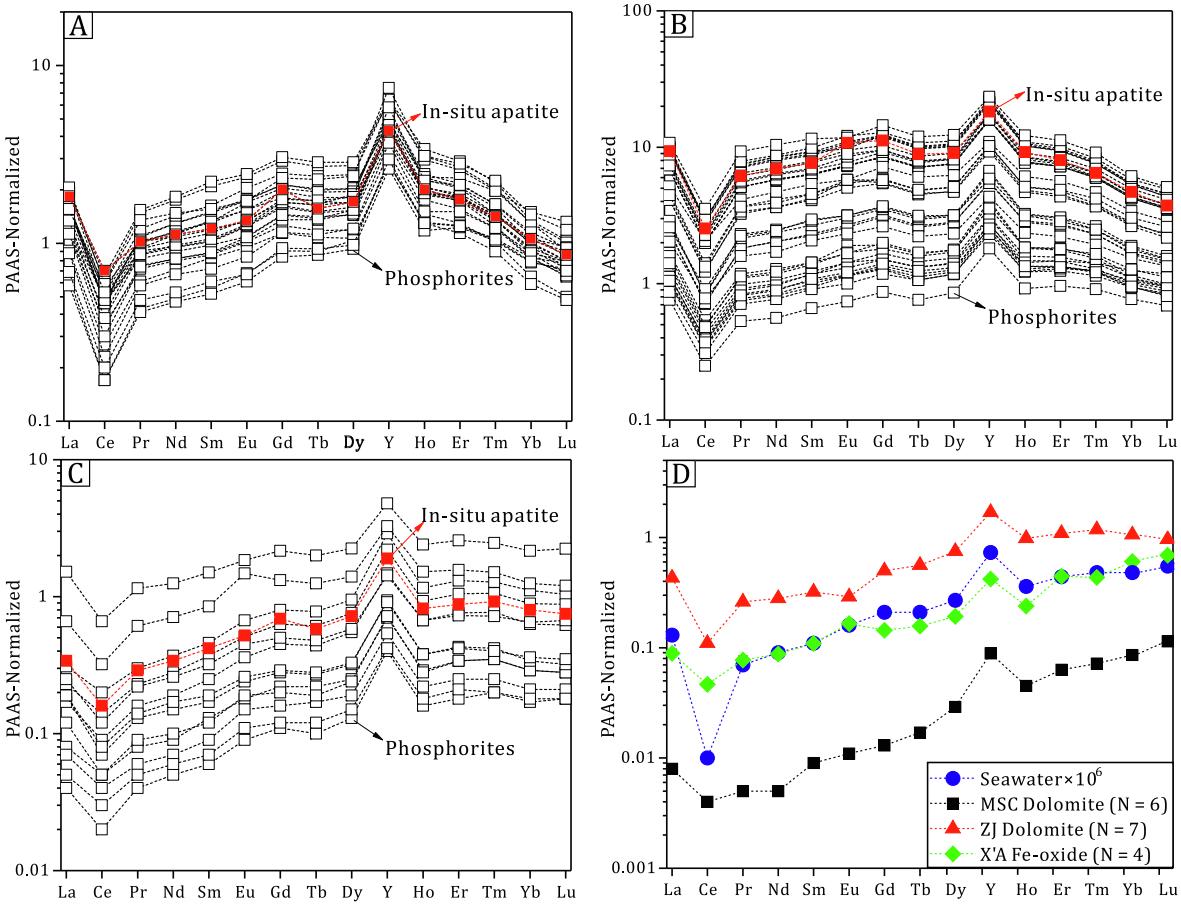


Fig. 6. The PAAS-normalized REY patterns of the Meishucun (A), Zhijin (B), and Xia'an (C) phosphorites, marked with average in-situ apatite data (red line). D. In-situ REY patterns of dolomite and Fe-oxide in the studied phosphorites compared with modern seawater (Alibo and Nozaki, 1999).

ter REY chemistry. However, in-situ dolomite in the MSC and ZJ phosphorites also show modern seawater-like REY patterns (Fig. 6), which indicates no obvious changes in seawater REY chemistry. The MREY-enriched REY patterns in the MSC and ZJ phosphorites can be ascribed to diagenetic alteration (discussed in Section 5.2.2). In addition, although the MSC and ZJ phosphorites are isochronous products, their REY abundances are fundamentally different. Therefore, different REY enrichment in the studied phosphorites cannot be attributed to changes in seawater REY chemistry.

In addition, post-depositional alteration, such as later hydrothermal activity and weathering processes, may change the REY abundance of the studied phosphorites. In the ZJ phosphorites, Xing et al. (2021) identified a group of hydrothermally transformed apatite grains through detailed mineral and geochemical work. However, the results showed that REY content in primary apatite grains and hydrothermally transformed apatite grains are identical, indicating that later hydrothermal activity made negligible contributions to the ZJ REY enrichment. On the other hand, REY migration during weathering remains controversial, both REY depletion and enrichment in weathered phosphorites have been reported in previous studies, possibly depending on specific weathering conditions and degrees (McArthur and Walsh 1984; Ismael, 2002; Gnandi and Tobschall, 2003). Nevertheless, weathering of phosphorites is commonly characterized by the appearance of abundant crandallites (Al-Ca-phosphate) (Bonnot-Courtois and Flicoteaux, 1989; Gnandi and Tobschall, 2003). However, crandallites were not observed in any groups of our phosphorites during SEM-EDS analysis, which denies strong weathering. Therefore, REY abundance and distribution in the studied phosphorites are dominated by initial chemical deposition rather than post-depositional alteration.

### 5.2. Diagenetic contributions to phosphorite REY enrichment

Phosphatized skeletons of modern organisms generally contain ΣREY concentrations at sub-ppm levels (Lécuyer et al., 1998; Kohn et al., 1999), whereas ΣREY concentrations in fossil bioapatite can reach thousands of ppm (Lécuyer et al., 1998; Liao et al., 2019). Additionally, the long-term open behavior of apatite grains with respect to REYs has been proposed in previous studies (Kocsis et al., 2010; Herwartz et al., 2011; Lumiste et al., 2019). Therefore, diagenetic REY uptake has been widely

employed to explain REY enrichment in bioapatite or phosphorites (Kocsis et al., 2010; Chen et al., 2015; Lumiste et al., 2019; Francovschi et al., 2020).

*5.2.1. Indications from mineralogy and elemental mapping*

Francolite represents the initial products of phosphate deposition despite that an amorphous precursor may be possible, which generally occurs as aggregates (apatite grains or structureless aggregates) in phosphorites, the mineralogical characteristics of which can provide broad information of diagenetic alteration (Föllmi, 1996; Ilyin, 1998). Generally, initially deposited francolites are poorly crystallized and stack as structureless aggregates (Gulbrandsen et al., 1984; Ilyin, 1998; Gunnars et al., 2004). During diagenetic alteration, francolite crystallizes better and may develop hexagonal-prism crystallites and tend to develop granular aggregates (Gulbrandsen et al., 1984; Ilyin, 1998). The francolites in the X'A phosphorites are characterized by obscure outlines and loosely stacked as amorphous aggregates (Fig. 3G-I and Supplementary Fig. S1), which may represent initially deposited phosphorites (Ilyin, 1998). In the MSC and ZJ phosphorites, however, francolites were well-crystallized with clear outlines (Fig. 3C and F) and tightly stacked as granular aggregates, mainly sub-rounded or fossil-shaped (Fig. 3A, B, D, and E). Collectively, these observations indicate that the X'A phosphorites may represent pristine phosphorites, whereas the MSC and ZJ phosphorites experienced intensive diagenetic alteration. In this case, the higher ΣREY concentrations in the MSC and ZJ phosphorites, relative to the X'A phosphorites, seemingly can be attributed to diagenetic REY enrichment. For example, in the Khubsugul Basin, pristine phosphorites deposited at the E-C boundary contain ΣREY at only 15–60 ppm, whereas granular and pelletal varieties contain much higher ΣREY at 578–650 ppm (Ilyin, 1998).

In addition, diagenetic REY uptake in apatite grains will be intensified by reworking owing to repeated exposure to surface REY-enriched porewater (Haley et al., 2004; Himmler et al., 2013; Abbott et al., 2015). The MSC phosphorites developed well-rounded apatite grains, in which smaller and sub-rounded grains are generally present, which may indicate strong reworking processes (Fig. 3A; Wen et al., 2011). In contrast, apatite grains in the ZJ phosphorites are either sub-rounded or fossil-shaped, without prominent mineralogical signs of reworking (Fig. 3D and E). On the other hand, apatite grains with frequent reworking generally tend to develop REY-enriched rims (within 10–20 μm) owing to long-term exposure to REY-enriched shallow porewater horizon (Lumiste et al., 2019). REY-enriched rims were indeed observed in the MSC phosphorites (Fig. 4A), indicating enhanced diagenetic uptake of REYs during reworking. The ZJ apatite grains, however, show a homogeneous REY distribution (Fig. 4B and Liu et al., 2020), similarly to the pristine X'A apatite aggregates (Fig. 4C), which demonstrates that diagenetic REY uptake in the ZJ phosphorites has not been enhanced by reworking. Nevertheless, although the MSC phosphorites may have experienced more intensive diagenetic REY uptake, the REYs in these phosphorites, even in the REY-enriched rims, are much lower than the REYs in the ZJ phosphorites (Fig. 4). Therefore, diagenetic alteration can explain the ΣREY enrichment in the MSC phosphorites (~200–400 ppm) relative to the pristine X'A phosphorites (mostly < 200 ppm), but it is not sufficient to explain the extraordinary ΣREY enrichment in the ZJ phosphorites (~500–2000 ppm).

*5.2.2. Indications from REY indexes*

Adsorption and substitution are the two main mechanisms for REY uptake in francolite during diagenesis. The adsorption mechanism is mainly associated with crystal surface control, which generally occurs during early diagenetic stage, whereas the substitution mechanism is mainly related to crystal structure control ($REY^{3+}$ substitution for $Ca^{2+}$), which generally occurs during late diagenetic stage with francolite recrystallization (Reynard et al., 1999; Liao et al., 2019). The adsorption mechanism preferentially assimilates LREYs and produces increasing $La_N/Yb_N$ ratios, whereas the substitution process preferentially utilizes MREYs and produces decreasing $La_N/Sm_N$ ratios (Koeppenkastrop and De Carlo, 1992; Reynard et al., 1999). The $La_N/Yb_N$ and $La_N/Sm_N$ values of the X'A phosphorites are mostly located within the modern seawater range (Fig. 7A), indicating the absence of diagenetic alteration, compatible with the mineralogical observations illustrated above. In contrast, although the $La_N/Sm_N$ values clustered within the seawater range, obviously enhanced $La_N/Yb_N$ values were observed in the MSC and ZJ phosphorites (Fig. 7A), indicating strong diagenetic adsorption of REYs. A positive correlation of the $La_N/Yb_N$ values and ΣREY concentrations in the studied phosphorites was observed (Fig. 7B), which validates diagenetic REY enrichment. However, the increase of ΣREY in the ZJ phosphorites is much sharper than the coupling trends of the X'A and MSC phosphorites (Fig. 7B), which may indicate additional control (redox control as discussed in Section 5.4) on the REY enrichment in the ZJ phosphorites.

The MREY-enriched REY pattern (PAAS-normalized) is prominent in the MSC and ZJ phosphorites (Fig. 6). Previous studies proposed that the MREY-enriched REY pattern was possibly inherited from contemporaneous seawater without net REY fractionation (Lécuyer et al., 2004; Emsbo et al., 2015). However, the pristine X'A phosphorites and in-situ dolomite in the MSC and ZJ phosphorites showed modern seawater-like REY patterns (Fig. 6), which denies that contemporaneous seawater is MREY-enriched. Another hypothesis is that the MREY-enriched REY pattern of phosphorites may be generated from diagenetic processes in porewater. Notably, modern-ocean sediments can develop both seawater-like porewater REYs and MREY-enriched porewater REYs (Haley et al., 2004; Kim et al., 2012). The seawater-normalized REY patterns in the MSC and ZJ phosphorites are obviously LREY-enriched (Fig. 7C), indicating that these phosphorites preferentially uptake LREYs if porewater REYs were seawater-like, which reconciles REY fractionation during diagenetic adsorption as discussed above (Fig. 7A). Therefore, the MREY-enriched REY pattern may result from REY fractionation during diagenetic adsorption (Haley et al., 2004;

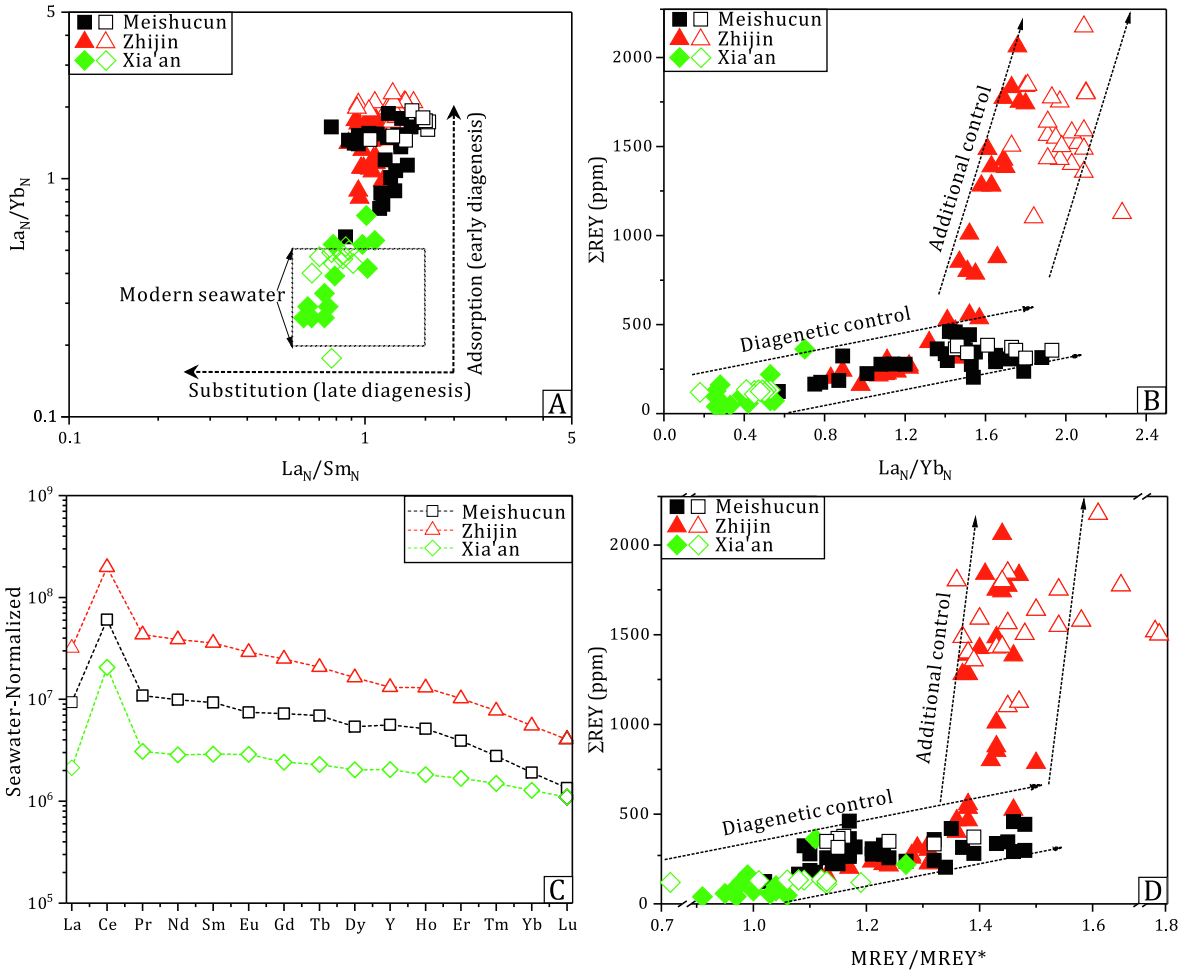


Fig. 7. The $La_N/Yb_N$ values plotted against $La_N/Sm_N$ values of the studied phosphorites (A), indicating that REYs in the Meishucun and Zhijin phosphorites were mainly captured by adsorption mechanism during early diagenesis. ΣREY plotted against $La_N/Yb_N$ values of the studied phosphorites (B), indicating that diagenesis cannot explain the extraordinary REY enrichment in the ZJ phosphorites (additional control points to redox control based on subsequent discussion). The seawater-normalized REY patterns of the studied phosphorites (C) (Alibo and Nozaki, 1999), indicating obvious LREY enrichment in the Meishucun and Zhijin phosphorites. ΣREY plotted against MREY/MREY* values of the studied phosphorites (D), indicating that diagenesis cannot explain the extraordinary REY enrichment in the ZJ phosphorites (additional control points to redox control based on subsequent discussion). The solid symbol represents bulk-rock data and the open symbol represents in-situ apatite data.

Kim et al., 2012). In addition, porewater can directly develop abnormal MREY enrichment through REY desorption from Fe-oxide (Haley et al., 2004) and possibly from organic matter (Felitsyn and Morad, 2002; Pi et al., 2013), which may alternatively result in MREY-enriched REY patterns in phosphorites if REY fractionation during diagenetic uptake was small. For example, Paul et al. (2019) found that modern apatite-bearing deep-sea sediments from central equatorial Pacific and porewater therein show similar MREY-enriched REY patterns. Regardless of the specific mechanism, the prominent MREY enrichment in the MSC and ZJ phosphorites may be ascribed to diagenetic REY enrichment. Notably, the MREY anomalies (MREY/MREY*) positively correlate with the ΣREY content in the studied phosphorites (Fig. 7D), validating diagenetic REY enrichment. However, the ZJ phosphorites are located out of the coupling trends of the MSC and X'A phosphorites (Fig. 7D), which again demonstrates additional control (redox control as discussed in Section 5.4) on the REY enrichment in the ZJ phosphorites.

Note that the ZJ phosphorites generally yield a much sharper increase in ΣREY than the MSC and X'A phosphorites during diagenetic REY uptake (Fig. 7 B and D), which generally occurs in porewater at the seawater-sediment interface (Lumiste et al., 2019). Previous studies have shown that the REY concentrations in modern ocean porewater can change by two orders of magnitude (Haley et al., 2004; Kim et al., 2012; Himmler et al., 2013; Abbott et al., 2015). Therefore, REY concentrations in porewater may significantly affect REY enrichment in phosphorites during diagenetic REY uptake. For example, Paul et al. (2019) proposed that diagenetic REY uptake into apatite grains in modern deep-sea muds can be obviously affected by REY availability in porewater. Porewater REYs

are mainly contributed by the decomposition of organic matter and reductive dissolution of Fe-oxide, but Fe-oxide reduction will dominate porewater REYs if it occurs (Haley et al., 2004). Also, organic matter and Fe-oxide control the phosphate concentrations in porewater (Föllmi, 1996), providing coupled cycling of REYs and phosphate near the seawater-sediment interface. The organic matter flux mainly depends on productivity levels, whereas Fe-oxide reduction is largely regulated by seawater redox conditions (Algeo et al., 2013; Johnson et al., 2020). Therefore, productivity levels and Fe redox cycling are discussed in the following two Sections.

### 5.3. Organic role in phosphorite REY enrichment

#### *5.3.1. Indications from petrography and TOC*

Biological activity can be tracked by fossil records in sediments. The early Cambrian small shelly fossils occurred in both the MSC and ZJ phosphorites, but the fossil abundance in the MSC phosphorites is rather limited (Fig. 3A). In the ZJ phosphorites, however, phosphatized small shelly fossils are much more abundant and even dominate the bulk-rock phosphate minerals in some samples (Fig. 3D; Mao et al., 2013). The relative fossil abundances may indicate that the biological activity is more intensive in the ZJ area than in the MSC location. Additionally, the X'A phosphorites are characterized by phosphatized (columnar) stromatolites (Fig. 3G; Zhang, 2016), which are generally formed by microbial phosphate accumulation (Krajewski et al., 2000; Caird et al., 2017). Collectively, the petrographic observations indicate that the ZJ and X'A phosphorites may have been formed under higher productivity levels than the MSC phosphorites. However, the X'A phosphorites were not mirrored by similarly high REY concentrations to the ZJ phosphorites, indicating that biological activity cannot explain the extraordinary REY enrichment in the ZJ phosphorites.

Generally, TOC in sediments is an important index for productivity levels (Algeo et al., 2013). However, the TOC in sediments is dictated not only by productivity levels but also by preservation in the water column and sediments (Schoepfer et al., 2015). In our phosphorites, the TOC is commonly low, mostly lower than 0.5%, particularly in the X'A phosphorites (Fig. 8A). The commonly low TOC in the studied phosphorites may reflect poor preservation under oxic–suboxic deposition conditions (see below) and thus cannot track different productivity levels. Nevertheless, positive correlations ($R^2 = 0.68$) between ΣREY and TOC have been observed in the early Cambrian phosphatic rocks from the Gorgan-Rasht Zone in northern Iran (Abedini and Calagari, 2017). However, although positive correlations can be observed, the TOC (0.5%–4.8%) and ΣREY (~100–300 ppm) in these phosphatic rocks are clustered within a narrow range (Fig. 8A). In contrast, although the ΣREY (231–1579 ppm) and TOC (1.0%–10.9%) change widely in the Permian Enoch Valley phosphorites (USA), no fair correlations have been observed (Piper, 1999) (Fig. 8A). Therefore, the role of biological productivity in REY enrichment in phosphorites remains controversial.

#### *5.3.2. Indications from Zn isotopes*

Zn involves several key physiological processes within phytoplankton cells (Sinoir et al., 2012); in particular, it functions as a cofactor in carbonic anhydrase, which is essential for carbon fixation (Morel et al., 1994). Consequently, Zn plays an important role in regulating marine productivity levels, which in turn affect oceanic Zn cycling (Weber et al., 2018; Sieber et al., 2020). However, the oceanic Zn cycling also involves other inorganic processes, mainly including Zn-sulfide precipitation and oxide particulate scavenging (Little et al., 2014; Vance et al., 2016). We did not find obvious Zn-sulfide in the studied phosphorites during SEM-EDS analysis, consistent with the lack of an Fe-sulfide phase (Fig. 3). If this is the case, Zn bonded with

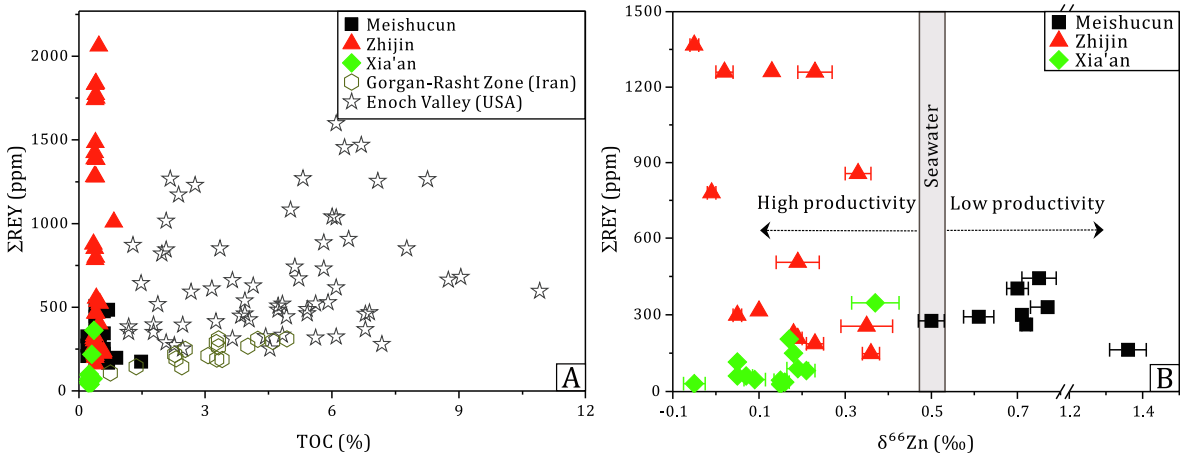


Fig. 8. ΣREY plotted against TOC of the studied and reported phosphorites (A), showing poor correlations between ΣREY and TOC. ΣREY plotted against $\delta^{66}Zn$ values of the studied phosphorites (B), indicating that productivity levels in the ZJ and X'A phosphorites are systematically higher than the MSC phosphorites. Data sources: Gorgan-Rasht Zone (Iran) (Abedini and Calagari, 2017) and Enoch Valley (USA) (Piper, 1999).

organic matter and Fe-oxide may be the major pathways for Zn precipitation (Little et al., 2014; Weber et al., 2018). In-situ data show that Zn abundance in apatite grains is ~6–10 times (average value) higher than that in dolomite (another major mineral phase in our phosphorites) (Table S2), indicating that apatite grains may be the major Zn carrier in phosphorites. The incorporation mechanisms of Zn into francolite are not well-understood, but an experimental study showed that $Zn^{2+}$ tends to enter the francolite lattice by replacing $Ca^{2+}$ during or immediately after francolite formation (Mayer et al., 1994).

Both experimental and natural observations found that Zn adsorbed onto Fe-Mn oxides is isotopically heavier than the initial solution ($\Delta^{66}Zn_{adsorbed\text{-}solution}$ = 0.16‰–0.61‰; Pokrovsky et al., 2005; Bryan et al., 2015). Additionally, theoretical calculations and modeling experiments indicated that phosphate preferentially complexes with isotopically heavy Zn ($\Delta^{66}Zn_{phosphate\text{-}solution}$ = 0.2‰–1.0‰; Fujii and Albarède, 2012; Veeramani et al., 2015). Together, if Zn in our phosphorites was predominantly transferred from the water column by Fe-Mn oxides, higher $\delta^{66}Zn$ values than those of bulk seawater can be expected. However, only the MSC phosphorites yield higher $\delta^{66}Zn$ values ($\delta^{66}Zn_{average}$ = 0.75‰) than those of bulk seawater (~0.50‰; Vance et al., 2016), whereas the ZJ and X'A phosphorites produce similarly low $\delta^{66}Zn$ values ($\delta^{66}Zn_{average}$ = 0.16‰ and 0.14‰, respectively; Fig. 8B). The $\delta^{66}Zn$ values in the MSC phosphorites ($\delta^{66}Zn_{average}$ = 0.75‰) are similar to those in the Ediacaran Weng'an phosphorites ($\delta^{66}Zn_{average}$ = 0.80‰), which were interpreted as Zn isotope fractionation during Zn complexation with phosphate and Zn adsorption onto Fe-Mn oxides and organism surfaces (Fan et al., 2018). If this is the case, the Zn isotope signals in the MSC phosphorites may be dominated by inorganic (Fe-oxide) scavenging, potentially indicating relatively low productivity levels.

The low $\delta^{66}Zn$ values in the ZJ and X'A phosphorites possibly result from the Zn biogeochemical cycling. Previous studies indicated that the biogeochemical cycling of Zn prevailing today may have been established since at least the Neoproterozoic (Pons et al., 2013; Fan et al., 2018; Isson et al., 2018). Generally, phytoplankton preferentially assimilates light Zn isotopes, although preferential uptake of heavy Zn isotopes is possible for specific conditions and species (Samanta et al., 2018; Köbberich and Vance, 2019). Isotope fractionation during biological uptake changes widely but mostly clusters within a narrow range ($\Delta^{66}Zn_{solution\text{-}phytoplankton}$ = 0.2‰–0.6‰; Samanta et al., 2018; Köbberich and Vance, 2019). The average $\delta^{66}Zn$ values in the ZJ and X'A phosphorites are similar to the modern organic-enriched shelf sediments (~0.0‰–0.2‰; Little et al., 2016). Given positive isotope fractionation during Zn uptake into francolite, the Zn isotope composition of the initial deposition flux in the ZJ and X'A areas may be negative, which indicates extremely high productivity levels. Therefore, the ZJ and X'A phosphorites may have experienced higher productivity than the MSC phosphorites, consistent with the petrographic observations illustrated above. However, the high-productivity X'A phosphorites yielded the lowest REY content among the studied phosphorites, indicating that the extraordinary REY enrichment in the ZJ phosphorites cannot be attributed to productivity control.

### 5.4. Redox controls on phosphorite REY enrichment

#### *5.4.1. Indications from REY indexes*

Y and Ho generally act as geochemical twins because they have very similar ionic radii and identical valences (Zhang et al., 1994; Pack et al., 2007). Therefore, Y and Ho are tightly coupled in many geological processes such as magmatic and hydrothermal activity, which generally maintains chondritic Y/Ho ratios (~25–30; Pack et al., 2007). However, marine behavior can significantly fractionate Y from Ho associated with preferential scavenging of Ho by suspended Fe-Mn oxides (Bau et al., 1997). Modern oxic seawater generally gives super-chondritic Y/Ho ratios, which mainly change from 50 to 70 (62 on average; Nozaki et al., 1997). However, the fractionation between Y and Ho will be discounted under anoxic conditions owing to the reductive dissolution of Fe-Mn oxides. For example, in the Tyro sub-basin, the Y/Ho ratio decreases from 55 in overlying oxic seawater to 36 in underlying anoxic brine (Bau et al., 1997). The Y/Ho ratios of the MSC and X'A phosphorites are 60 ± 5.0 and 64 ± 4.5, respectively, which correspond with well-oxygenated seawater (Nozaki et al., 1997). In contrast, the ZJ phosphorites yield slightly lower Y/Ho ratios (54 ± 2.5; Fig. 5B), which may indicate suboxic seawater conditions. Recently, based on redox-sensitive elements, Zhang et al. (2021) also proposed that the ZJ phosphorites were deposited in an oxygen-poor seawater environment. Under suboxic seawater conditions, high dissolved Fe levels in seawater and favorable reductive dissolution of Fe-oxide in anoxic sediments can be expected. For example, in modern marine sediments, porewater with the occurrence of dissolved Fe generally contains REY content several times higher than that in porewater without dissolved Fe present (Haley et al., 2004). If true, the ZJ porewater may have maintained higher REY levels than the MSC and X'A porewater. This hypothesis can be supported by the ΣREY gradients of in-situ dolomite in the studied phosphorites, in which the ZJ dolomite yields much higher ΣREY content (56–139 ppm) than the MSC (3–5 ppm) and X'A dolomite (<1 ppm) (Table S2). Therefore, higher porewater REYs driven by frequent Fe redox cycling may be the major reason for the extraordinary REY enrichment in the ZJ phosphorites, which can be further validated by the following Fe isotope discussion.

A recent study found that, within single phosphorite deposits in eastern Algeria, phosphorites with less negative Ce anomalies generally contain higher REY content, indicating more favorable REY enrichment in phosphorites under suboxic conditions (Kechiched et al., 2020). In our phosphorites, however, ΣREY content is poorly correlated with Ce anomalies (Fig. 9A). Pr/Pr* parameter can distinguish real Ce anomalies from fake ones because of the overabundances of La (Bau and Dulski, 1996). However, Fig. 9B showed that the Ce anomalies in the studied phosphorites are real. The average Ce/Ce* values are 0.39, 0.33,

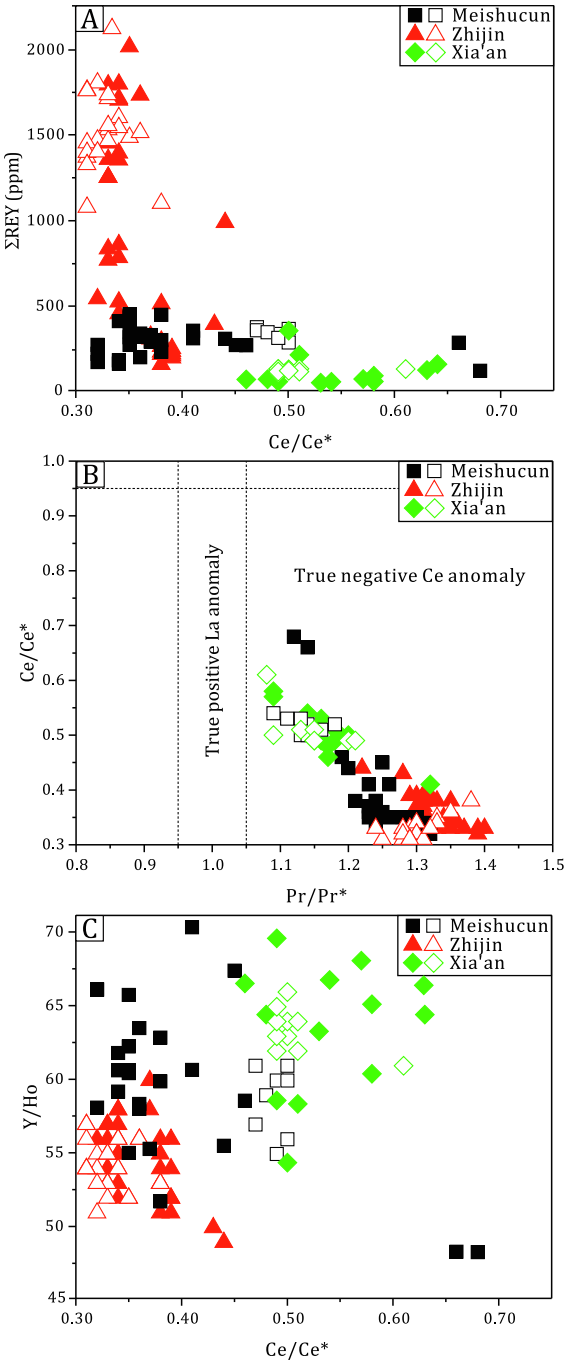


Fig. 9. ΣREY plotted against Ce/Ce* values (A), Ce/Ce* values plotted against Pr/Pr* values (B) and Y/Ho values (C) of the studied phosphorites. The lack of negative correlations between the Y/Ho values and Ce/Ce* values may indicate that phosphorite Ce/Ce* values were not determined by seawater redox conditions. The solid symbol represents bulk-rock data and the open symbol represents in-situ apatite data.

and 0.54 in the MSC, ZJ, and X'A phosphorites, respectively, which appears to reflect overall oxic deposition environments (particularly for the MSC and ZJ phosphorites) (German et al., 1991; Alibo and Nozaki, 1999). However, many studies have questioned the use of phosphorite Ce anomalies as a redox proxy because Ce anomalies in francolite may also involve REY fractionation during diagenetic uptake and relate to porewater REY chemistry (Shields and Stille, 2001; Herwartz et al., 2011; Liao et al., 2019). This discipline may be effective for our phosphorites, as indicated by the poor correlations between the Ce/Ce* values and Y/Ho ratios (Fig. 9C). For example, an experimental study showed that Ce has a lower distribution coefficient than its neighboring La and Pr during REY adsorption onto phosphate mineral phases (Koeppenkastrop and De Carlo, 1992). As discussed above (Section 5.2.2), diagenetic adsorption may dominate the REY enrichment in the MSC and ZJ phosphorites. Therefore, the similarly low Ce/Ce* values in the MSC and ZJ phosphorites may result from REY fractionation during diagenetic uptake and not necessarily reflect more oxic deposition conditions than the X'A phosphorites. Alternatively, the similarly low Ce/Ce* values in the MSC and ZJ phosphorites may be generated from Ce-depleted porewater induced by REY cycling in porewater, such as in modern apatite-bearing deep-sea sediments (Paul et al., 2019). Therefore, Ce anomalies in our phosphorites may not only be controlled by seawater redox conditions and thus could not be employed to constrain the redox history of the studied phosphorites.

### 5.4.2. Indications from Fe isotopes

The isotopic composition of Fe in marine sediments provides the most direct indication of the Fe redox cycling (Li et al., 2013; Fan et al., 2014; Kunzmann et al., 2017; Johnson et al., 2020). However, mixing of different Fe minerals in bulk-rock sediments may obscure redox-dependent Fe isotope signals owing to different Fe minerals yielding different Fe isotope compositions (Fan et al., 2014; Johnson et al., 2020). Generally, Fe-oxide, Fe-sulfide, Fe-carbonate, and Fe-silicate are together responsible for the bulk-rock $\delta^{56}$Fe values. Firstly, we did not digest the silicate fraction during Fe-isotope chemical purification; thus, Fe-silicate makes no contributions to the bulk-rock $\delta^{56}$Fe values. In addition, SEM examination validates that Fe-oxide dominates the Fe-mineral phase in our phosphorites (Fig. 3), pyrite (Fe-sulfide) was only observed in a few ZJ and X'A phosphorites in minor amounts, indicating that Fe-oxide may dominate the bulk-rock $\delta^{56}$Fe values. However, Fan et al. (2016) found that Fe-carbonate is another important Fe fraction in phosphorites, which can reach ~30% despite being in near-pure phosphorites ($P_2O_5$ > 15%). Therefore, it is possible that the bulk-rock $\delta^{56}$Fe values in some phosphatized dolostones ($P_2O_5$ < 15% and MgO > 10%) are dominated by Fe-carbonate instead of Fe-oxide, although isolated Fe-carbonate mineral cannot be observed during SEM observations.

In the studied phosphorites, Fe-oxide mainly occurs in the interior of apatite or dolomite grains (Fig. 3), indicating that Fe-oxide was deposited simultaneously with phosphorites rather than from later hydrothermal activity. In this situation, the $\delta^{56}$Fe values of sedimentary Fe-oxide are largely determined by Fe isotope fractionation during redox transformation from $Fe^{2+}$-solution to $Fe^{3+}$-oxide. Experi-

mental studies demonstrated that $Fe^{3+}$ precipitates preferentially utilize heavier Fe isotopes than the initial $Fe^{2+}$-solution by biotic and abiotic oxidation processes ($\Delta^{56}Fe_{Fe\text{-}oxide\text{-}solution}$ = 0.9‰–3.0‰; Welch et al., 2003; Swanner et al., 2015; Wu et al., 2017). Under well-oxygenated environments, however, quantitative Fe oxidation masks Fe isotope fractionation and produces Fe-oxide with similar $\delta^{56}$Fe values to ambient seawater (~0.0‰; Johnson et al., 2008). However, partial $Fe^{2+}$ oxidation under ferruginous or suboxic conditions generally produces positive $\delta^{56}$Fe values in deposited Fe-oxide (Li et al., 2013). The MSC and X'A bulk-rocks (dominated by near-pure phosphorites) are characterized by ~0‰ $\delta^{56}$Fe values (Fan et al., 2016), indicating that these phosphorites were deposited under well-oxygenated environments (Fig. 10A). The $\delta^{56}$Fe values in the ZJ phosphorites show a bimodal distribution, which may depend on the relative fractions of Fe-carbonate and Fe-oxide. Phosphatized dolostones commonly produce negative $\delta^{56}$Fe values (−0.54‰ to −0.10‰; Fig. 10A), which may reflect a significant Fe-carbonate fraction ($Fe^{2+}$), generally enriched in light Fe isotopes ($\delta^{56}$Fe = ~−0.6‰; Fan et al., 2016; Yang et al., 2018b). However, the near-pure phosphorites are characterized by positive $\delta^{56}$Fe values (~0.0‰ to 0.45‰; Fig. 10A), which may be attributed to partial $Fe^{2+}$ oxidation and deposition under ferruginous or suboxic seawater conditions. Partial $Fe^{2+}$ oxidation has also been applied to explain the positive $\delta^{56}$Fe values of the E-C boundary shales and cherts (Fan et al., 2014; Kunzmann et al., 2017).

The varied $\delta^{56}$Fe values of ~0.0‰–0.45‰ in the near-pure ZJ phosphorites may indicate fluctuating oxic–suboxic seawater conditions. In this situation, high dissolved $Fe^{2+}$ levels can be expected in a suboxic seawater column but the dissolved $Fe^{2+}$ can be rapidly oxidized to Fe-oxide when an oxic seawater column dynamically occurred (Scholz et al., 2014; Yang et al., 2018b). Meanwhile, the reductive dissolution of Fe-oxide is favorable in anoxic porewater, particularly when the sediments were overlain by a suboxic seawater column (Severmann et al., 2008; Scholz et al., 2014). Therefore, the fluctuating oxic–suboxic conditions may have promoted extensive Fe redox cycling near the seawater-sediment interface. Notably, reductive dissolution of Fe-oxide may induce partial loss of isotopically light $Fe^{2+}$ (Fe shuttle), leaving sediments with higher $\delta^{56}$Fe values (Severmann et al., 2008; Scholz et al., 2014). Therefore, the positive $\delta^{56}$Fe values in the near-pure ZJ phosphorites can be alternatively ascribed to intensive Fe redox cycling, although this process generally elevates bulk-rock $\delta^{56}$Fe values by < 0.2‰ (Severmann et al., 2008; Scholz et al., 2014). The Fe shuttle process can be determined by the correlation between $\delta^{56}$Fe values and Fe/Al ratios (Severmann et al., 2008). No correlations were observed in the MSC and X'A phosphorites, indicating a weak Fe shuttle, whereas the ZJ phosphorites showed two major coupling trends (Group Ⅰ and Group Ⅱ; Fig. 10B). Group Ⅰ is dominated by phosphatized dolostones and characterized by negative $\delta^{56}$Fe values, and the coupling trend may predominately reflect varied proportions between Fe-carbonate and Fe-oxide. Group Ⅱ is dominated by near-pure phosphorites, and the negative correlation of the $\delta^{56}$Fe value with the Fe/Al ratio indicates that these phosphorites may have experienced intensive Fe redox cycling.

Importantly, Fe redox cycling can significantly enrich porewater with REYs (Haley et al., 2004), which can be subsequently captured into francolite during its formation and early diagenesis (Kashiwabara et al., 2018). The extremely low ΣREY content of in-situ Fe-oxide in our phosphorites may support this scenario (<1–48 ppm; Table S2). For example, modern Fe-Mn crusts generally contain ΣREY at hundreds of ppm (Yasukawa et al., 2020), whereas Fe-oxide in modern deep-sea sediments with the occurrence of REY-enriched apatite contains ΣREY at similar levels to the Fe-oxide in our phosphorites (Paul et al., 2019). These observations possibly indicate that porewater REYs released by Fe-oxide can be largely assimilated by francolite during its formation and subsequent diagenesis, leaving the remained Fe-oxide with low REY content.

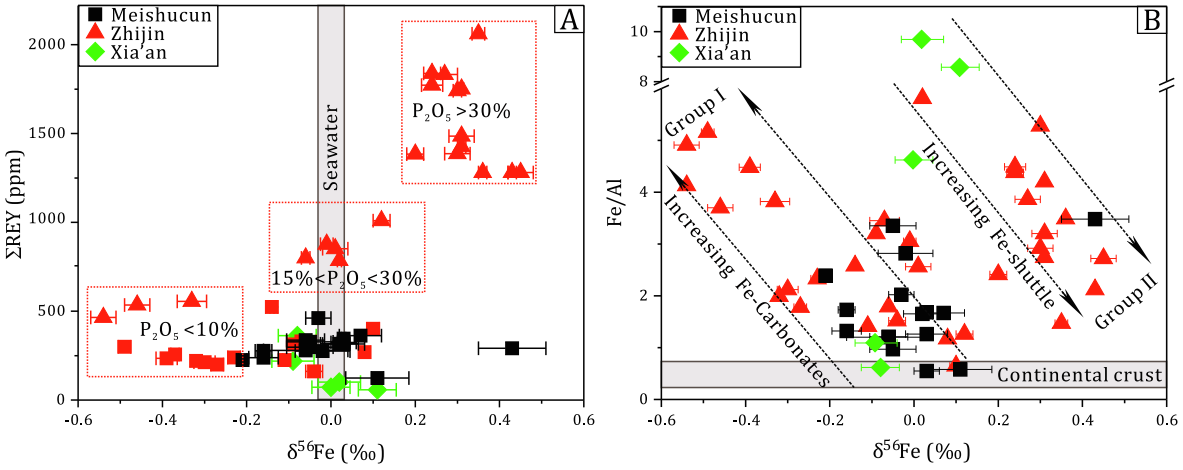


Fig. 10. ΣREY plotted against $\delta^{56}$Fe values (A) and Fe/Al ratios plotted against $\delta^{56}$Fe values (B) of the studied phosphorites, indicating that REY-enriched ZJ phosphorites were deposited under fluctuating oxic–suboxic deposition environments, in which intensive Fe redox cycling occurred.

As discussed above, the ZJ phosphorites may have experienced more extensive Fe redox cycling than the MSC and X'A phosphorites. It can be expected that, therefore, the REY content in ZJ porewater was much higher than that in the MSC and X'A porewater, which can be validated by the ΣREY gradients in in-situ dolomite (56–139 ppm in ZJ, 3–5 ppm in MSC, and < 1 ppm in X'A). If this is the case, frequent Fe redox cycling near the seawater-sediment interface driven by dynamic oxic–suboxic conditions may be the major reason for the extraordinary REY enrichment in the ZJ phosphorites.

### 5.5. Implication for the formation of phosphorite-type REY resources

During the early Cambrian, the Nanhua Basin was characterized by stratified redox conditions, in which oxic seawater dominated shallow shelf locations, below which seawater was mainly suboxic or ferruginous (Feng et al., 2014; Wen et al., 2015; Xiang et al., 2020; Zhang et al., 2020). Meanwhile, widespread phosphorites were deposited on the Yangtze Block; these phosphorites show systematic spatial changes in phosphorite scale and REY abundance (Fig. 11). Large-scale phosphorites mainly developed in inner-shelf environments, which generally yielded moderate ΣREY enrichment of ~200–400 ppm; examples are the MSC, LB, and MB phosphorites (Ou, 2015). The relative REY enrichment in the inner-shelf phosphorites can be largely ascribed to diagenetic REY uptake that may have been enhanced by reworking under dynamic seawater conditions, such as the studied MSC phosphorites. However, because well-oxygenated seawater may have limited the Fe redox cycling near the seawater-sediment interface in inner-shelf locations, the inner-shelf phosphorites generally cannot develop extraordinary REY enrichment although they are typically large-scale (Figs. 1 and 11).

A few large-scale phosphorites occurred in outer-shelf settings; examples are the ZJ and X'A phosphorites. The X'A phosphorites contain extremely low ΣREY (mostly < 200 ppm), which may be ascribed to the lack of both diagenetic REY uptake because of limited diagenetic alteration and Fe redox cycling because of well-oxygenated deposition conditions. Notably, the ZJ phosphorites yielded extraordinary ΣREY enrichment (~500–2 000 ppm). In particular, fluctuating oxic–suboxic seawater conditions locally developed at the outer-shelf ZJ location, which may reflect spatially heterogeneous redox conditions at this time (Wen et al., 2015; Zhang et al., 2020). Alternatively, the fluctuating oxic–suboxic deposition environments in the ZJ area were controlled by a local shelf basin, which can be supported by the fact that nearby phosphorite sediments in Guizhou are generally much thinner with small scales (Chen et al., 2013). Importantly, extensive Fe redox cycling near the seawater-sediment interface can be expected under fluctuating oxic-suboxic deposition conditions, which may have dominated the extraordinary REY enrichment in the ZJ phosphorites. This is because frequent Fe-redox cycling can significantly enrich REYs in porewater, which can be subsequently assimilated by francolite during its formation and early diagenesis.

In addition, small-scale concretionary phosphorites are widespread along or close to the slope belt (Fig. 11); examples are the phosphate concretions in the Daotuo, Rongxi, Longbizui, Sancha, Tianzhu, Bahuang, Shangrao, and

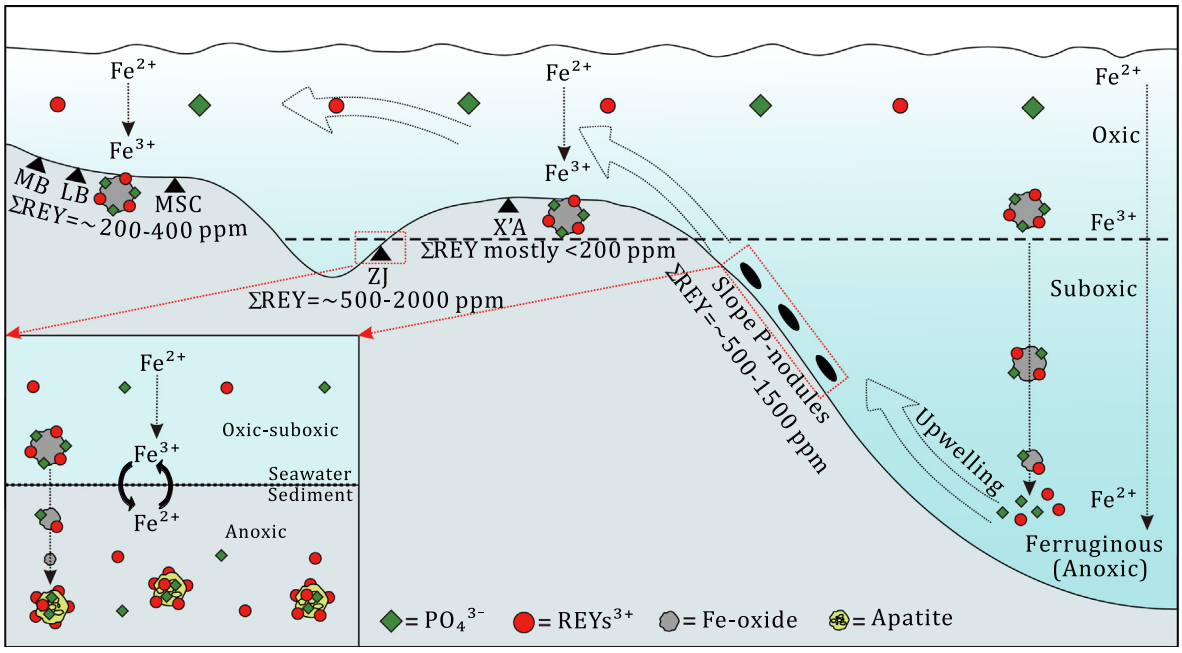


Fig. 11. Simple conceptual figure of REY and phosphate cycling associated with Fe-oxide in the redox-stratified Nanhua Basin during the early Cambrian. Note that the ZJ phosphorites and the near-slope P-nodules were formed under fluctuating oxic–suboxic deposition conditions, in which Fe redox cycling between seawater and sediments may be frequent. MSC-Meishucun (here), ZJ-Zhijin (here), X'A-Xia'an (here), LB-Leibo (Ou, 2015), MB-Mabian (Ou, 2015), Slope P-nodules (Chen et al., 2013; Zhu et al., 2014; Gao et al., 2018; Ye et al., 2021).

Nanjing areas (Chen et al., 2013; Zhu et al., 2014; Gao et al., 2018; Ye et al., 2021). Interestingly, these near-slope phosphate concretions generally contain high ΣREY content (~500–1500 ppm), comparable to that of the ZJ phosphorites (Fig. 11; Chen et al., 2013; Zhu et al., 2014; Gao et al., 2018; Ye et al., 2021), although local low-REY phosphate nodules have also been observed (Jiang et al., 2007; Ye et al., 2020). During the early Cambrian, suboxic or ferruginous seawater conditions may have dominated the slope-basin locations (Feng et al., 2014; Wen et al., 2015; Xiang et al., 2020; Zhang et al., 2020). In this situation, the REY enrichment in the slope phosphate concretions may result from intensive Fe redox cycling driven by fluctuating oxic-suboxic deposition conditions, similarly to the ZJ phosphorites, although the isochronous deposition of these phosphate concretions and the ZJ phosphorites may not be strict. Collectively, the extensive Fe redox cycling driven by fluctuating oxic-suboxic deposition conditions may have dominated the extraordinary REY enrichment in the early Cambrian ZJ phosphorites and slope phosphate concretions on the Yangtze Block.

Similarly, apatite grains in the ~2–1.9 Ga phosphatic sediments in Russia yielded extremely high ΣREY (can reach several thousand ppm), for which fluctuating suboxic to anoxic deposition conditions were recognized by Ce/Ce* values and Y/Ho ratios (Joosu et al., 2015, 2016). In addition, ΣREY content is rather high in the Cretaceous–Paleogene boundary Abu Tartur phosphorites in Egypt (~500–1100 ppm), in which frequent Fe redox cycling was supported by the occurrence of abundant diagenetic pyrite (Ismael, 2002; Awadalla, 2010; Baioumy, 2011). Moreover, Algabri et al. (2020) demonstrated that the formation of glauconite may be associated with intensive Fe redox cycling under suboxic deposition conditions near the seawater-sediment interface. Notably, they found that apatite grains in glauconite-enriching phosphorites contained much higher ΣREY (~500–1000 ppm) than those in phosphorites with less or no glauconite composition (~100–300 ppm). In summary, the Fe redox pumping model established by our Fe isotopes may have universal indications for the extraordinary REY enrichment in phosphorites or phosphatic rocks.

## 6. CONCLUSIONS

In this study, three early Cambrian phosphorite deposits from South China with systematically varied REY content were investigated with mineralogy, bulk-rock elements, TOC, in-situ elements, and Zn-Fe isotopes to understand the origin of REY-enriched phosphorites. Diagenetic processes, biological activity, and seawater redox conditions were particularly focused. Our results indicate that diagenetic alteration promoted ΣREY enrichment in the MSC phosphorites (~200–400 ppm) relative to the pristine X'A phosphorites (mostly < 200 ppm), but it is not sufficient to explain the extraordinary ΣREY enrichment in the ZJ phosphorites (~500–2000 ppm). Productivity levels also cannot explain the extraordinary ZJ REY enrichment, although ZJ productivity levels are high, because the high-productivity X'A phosphorites yielded extremely low REY content. Notably, compared to the MSC and X'A phosphorites, the ZJ phosphorites may have experienced more intensive Fe redox cycling near the seawater-sediment interface driven by fluctuating oxic-suboxic redox conditions. Extensive Fe redox cycling can significantly enrich porewater with REYs, which can be subsequently captured by francolite during its formation and early diagenesis. Therefore, intensive Fe redox cycling driven by fluctuating oxic-suboxic redox conditions may be the dominant reason for the extraordinary REY enrichment in the ZJ phosphorites. Combined with previous studies, the Fe-redox pumping model could also have significantly stimulated extraordinary REY enrichment in other phosphorites or phosphatic rocks formed in different basins at different geological times.

## Declaration of Competing Interest

The authors declare that they have no known competing financial interests or personal relationships that could have appeared to influence the work reported in this paper.


## ACKNOWLEDGEMENTS

This work was funded by NSFC (9206220039, U1812402, 41890840, 4207030265, 42121003, 41773015) and the CAS IIT (JCTD-2019-17). We give thanks to the three anonymous reviewers and two editors for providing priceless comments and suggestions.


## APPENDIX A. SUPPLEMENTARY DATA

Supplementary data to this article can be found online at https://doi.org/10.1016/j.gca.2022.03.003.

## REFERENCES


Abbott A. N., Haley B. A., McManus J. and Reimers C. E. (2015) The sedimentary flux of dissolved rare earth elements to the ocean. *Geochim. Cosmochim. Acta* **154**, 186–200.

Abedini A. and Calagari A. A. (2017) REEs geochemical characteristics of lower Cambrian phosphatic rocks in the Gorgan-Rasht Zone, northern Iran: Implications for diagenetic effects and depositional conditions. *J. Afr. Earth Sci.* **135**, 115–124.

Algabri M., She Z., Jiao L., Papineau D., Wang G., Zhang C., Tang D., Ouyang G., Zhang Y., Chen G. and Li C. (2020) Apatite-glaucony association in the ediacaran doushantuo formation, south china and implications for marine redox conditions. *Precambrian Res.* **347** 105842.

Algeo T. J., Henderson C. M., Tong J., Feng Q., Yin H. and Tyson R. V. (2013) Plankton and productivity during the Permian-Triassic boundary crisis: An analysis of organic carbon fluxes. *Global Planet Change* **105**, 52–67.

Alibo D. S. and Nozaki Y. (1999) Rare earth elements in seawater: particle association, shale-normalization, and Ce oxidation. *Geochim. Cosmochim. Acta* **63**, 363–372.

Awadalla G. S. (2010) Geochemistry and microprobe investigations of Abu Tartur REE-bearing phosphorite, Western Desert. *Egypt. J. Afr. Earth Sci.* **57**, 431–443.

Baioumy H. (2011) Rare earth elements and sulfur and strontium isotopes of upper Cretaceous phosphorites in Egypt. *Cretaceous Res.* **32**, 368–377.

Balaram V. (2019) Rare earth elements: A review of applications, occurrence, exploration, analysis, recycling, and environmental impact. *Geosci. Front.* **10**, 1285–1303.

Banerjee S., Choudhury T. R., Saraswati P. K. and Khanolkar S. (2020) The formation of authigenic deposits during Paleogene warm climatic intervals: a review. *J. Palaeogeogr.* **9**(4), 1–27.

Bau M., Möller P. and Dulski P. (1997) Yttrium and lanthanides in eastern Mediterranean seawater and their fractionation during redox-cycling. *Mar. Chem.* **56**, 123–131.

Bau M. and Dulski P. (1996) Distribution of yttrium and rare-earth elements in the Penge and Kuruman iron-formations, Transvaal Supergroup. *South Africa. Precambrian Res.* **79**, 37–55.

Binnemans K., Jones P. T., Müller T. and Yurramendi L. (2018) Rare Earths and the Balance Problem: How to Deal with Changing Markets? *J. Sustain. Metall.* **4**, 126–146.

Bonnot-Courtois C. and Flicoteaux R. (1989) Distribution of rare-earth and some trace elements in Tertiary phosphorites from the Senegal Basin and their weathering products. *Chem. Geol.* **75**, 311–328.

Bryan A. L., Dong S., Wilkes E. B. and Wasylenki L. E. (2015) Zinc isotope fractionation during adsorption onto Mn oxyhydroxide at low and high ionic strength. *Geochim. Cosmochim. Acta* **157**, 182–197.

Buccione R., Kechiched R., Mongelli G. and Sinisi R. (2021) REEs in the North Africa P-Bearing Deposits, Paleoenvironments, and Economic Perspectives: A Review. *Minerals.* **11**, 214.

Caird R. A., Pufahl P. K., Hiatt E. E., Abram M. B., Rocha A. J. D. and Kyser T. K. (2017) Ediacaran stromatolites and intertidal phosphorite of the Salitre Formation, Brazil: Phosphogenesis during the Neoproterozoic Oxygenation Event. *Sediment Geol.* **350**, 55–71.

Chen J., Algeo T. J., Zhao L., Chen Z., Cao L., Zhang L. and Li Y. (2015) Diagenetic uptake of rare earth elements by bioapatite, with an example from Lower Triassic conodonts of South China. *Earth-Sci. Rev.* **149**, 181–202.

Chen J., Yang R., Wei H. and Gao J. (2013) Rare earth element geochemistry of Cambrian phosphorites from the Yangtze Region. *J. Rare Earths* **31**, 101–112.

Emsbo P., McLaughlin P. I., Breit G. N., du Bray E. A. and Koenig A. E. (2015) Rare earth elements in sedimentary phosphate deposits: Solution to the global REE crisis? *Gondwana Res.* **27**, 776–785.

Fan H. F., Wen H. J., Xiao C. Y., Zhou T., Cloquet C. and Zhu X. K. (2018) Zinc Geochemical Cycling in a Phosphorus-Rich Ocean During the Early Ediacaran. *J. Geophys. Res. Oceans* **123**, 5248–5260.

Fan H. F., Wen H. J. and Zhu X. K. (2016) Marine redox conditions in the Early Cambrian ocean: Insights from the Lower Cambrian phosphorite deposits. *South China. J. Earth Sci.* **27**, 282–296.

Fan H., Zhu X., Wen H., Yan B., Li J. and Feng L. (2014) Oxygenation of Ediacaran Ocean recorded by iron isotopes. *Geochim. Cosmochim. Acta* **140**, 80–94.

Felitsyn S. and Morad S. (2002) REE patterns in latest Neoproterozoic–early Cambrian phosphate concretions and associated organic matter. *Chem. Geol.* **187**, 257–265.

Feng L. J., Li C., Huang J., Chang H. J. and Chu X. L. (2014) A sulfate control on marine mid-depth euxinia on the early Cambrian (ca. 529–521Ma) Yangtze platform. *South China. Precambrian Res.* **246**, 123–133.

Föllmi K. B. (1996) The phosphorus cycle, phosphogenesis and marine phosphate-rich deposits. *Earth-Sci. Rev.* **40**, 55–124.

Francovschi I., Grădinaru E., Roban R., Ducea M. N., Ciobotaru V. and Shumlyanskyy L. (2020) Rare earth element (REE) enrichment of the late Ediacaran Kalyus Beds (East European Platform) through diagenetic uptake. *Geochemistry* **80** 125612.

Fujii T. and Albarède F. (2012) Ab initio calculation of the Zn isotope effect in phosphates, citrates, and malates and applications to plants and soil. *PLoS ONE* **7** e30726.

Gao P., He Z., Li S., Lash G. G., Li B., Huang B. and Yan D. (2018) Volcanic and hydrothermal activities recorded in phosphate nodules from the Lower Cambrian Niutitang Formation black shales in South China. *Palaeogeogr. Palaeoclimatol. Palaeoecol.* **505**, 381–397.

German C. R., Holliday B. P. and Elderfield H. (1991) Redox cycling of rare earth elements in the suboxic zone of the Black Sea. *Geochim. Cosmochim. Acta* **55**, 3553–3558.

Gnandi K. and Tobschall H. J. (2003) Distribution patterns of rare-earth elements and uranium in tertiary sedimentary phosphorites of Hahotoé-Kpogamé. *Togo. J. Afr. Earth Sci.* **37**, 1–10.

Gómez-Peral L. E., Kaufman A. J. and Poiré D. G. (2014) Paleoenvironmental implications of two phosphogenic events in Neoproterozoic sedimentary successions of the Tandilia System, Argentina. *Precambrian Res.* **252**, 88–106.

Gulbrandsen R. A., Roberson C. E. and Neil S. T. (1984) Time and the crystallization of apatite in seawater. *Geochim. Cosmochim. Acta* **48**, 213–218.

Gunnars A., Blomqvist S. and Martinsson C. (2004) Inorganic formation of apatite in brackish seawater from the Baltic Sea: an experimental approach. *Mar. Chem.* **91**, 15–26.

Haley B. A., Klinkhammer G. P. and McManus J. (2004) Rare earth elements in pore waters of marine sediments. *Geochim. Cosmochim. Acta* **68**, 1265–1279.

Herwartz D., Tütken T., Münker C., Jochum K. P., Stoll B. and Sander P. M. (2011) Timescales and mechanisms of REE and Hf uptake in fossil bones. *Geochim. Cosmochim. Acta* **75**, 82–105.

Himmler T., Haley B. A., Torres M. E., Klinkhammer G. P., Bohrmann G. and Peckmann J. (2013) Rare earth element geochemistry in cold-seep pore waters of Hydrate Ridge, northeast Pacific Ocean. *Geo-Mar Lett.* **33**, 369–379.

Hoshino M., Sanematsu K. and Watanabe Y. (2016) REE Mineralogy and Resources. *Handbook on the Physics and Chemistry of Rare Earths.* **49**, 129–291.

Ilyin A. V. (1998) Rare-earth geochemistry of 'old' phosphorites and probability of syngenetic precipitation and accumulation of phosphate. *Chem. Geol.* **144**, 243–256.

Ismael I. S. (2002) Rare earth elements in Egyptian phosphorites. *Chin. J. Geochem.* **21**, 19–28.

Isson T. T., Love G. D., Dupont C. L., Reinhard C. T., Zumberge A. J., Asael D., Gueguen B., McCrow J., Gill B. C., Owens J., Rainbird R. H., Rooney A. D., Zhao M., Stueeken E. E., Konhauser K. O., John S. G., Lyons T. W. and Planavsky N. J. (2018) Tracking the rise of eukaryotes to ecological dominance with zinc isotopes. *Geobiology* **16**, 341–352.

Jiang S., Zhao H., Chen Y., Yang T., Yang J. and Ling H. (2007) Trace and rare earth element geochemistry of phosphate nodules from the lower Cambrian black shale sequence in the Mufu Mountain of Nanjing, Jiangsu province. *China. Chem. Geol.* **244**, 584–604.

Johnson C. M., Beard B. L., Klein C., Beukes N. J. and Roden E. E. (2008) Iron isotopes constrain biologic and abiologic processes in banded iron formation genesis. *Geochim. Cosmochim. Acta* **72**, 151–169.

Johnson C., Beard B. and Weyer S. (2020) *Iron Geochemistry: An Isotopic Perspective*. Springer International Publishing: Cham, Switzerland, 2020; ISBN 978-3-030-33827-5.

Joosu L., Lepland A., Kirsimäe K., Romashkin A. E., Roberts N. M. W., Martin A. P. and Črne A. E. (2015) The REE-composition and petrography of apatite in 2Ga Zaonega Formation, Russia: The environmental setting for phosphogenesis. *Chem. Geol.* **395**, 88–107.

Joosu L., Lepland A., Kreitsmann T., Üpraus K., Roberts N. M. W., Paiste P., Martin A. P. and Kirsimäe K. (2016) Petrography and the REE-composition of apatite in the Paleoproterozoic Pilgujärvi Sedimentary Formation, Pechenga Greenstone Belt, Russia. *Geochim. Cosmochim. Acta* **186**, 135–153.

Kato Y., Fujinaga K., Nakamura K., Takaya Y., Kitamura K., Ohta J., Toda R., Nakashima T. and Iwamori H. (2011) Deep-sea mud in the Pacific Ocean as a potential resource for rare-earth elements. *Nat. Geosci.* **4**, 535–539.

Kashiwabara T., Toda R., Nakamura K., Yasukawa K., Fujinaga K., Kubo S., Nozaki T., Takahashi Y., Suzuki K. and Kato Y. (2018) Synchrotron X-ray spectroscopic perspective on the formation mechanism of REY-rich muds in the Pacific Ocean. *Geochim. Cosmochim. Acta* **240**, 274–292.

Kechiched R., Laouar R., Bruguier O., Kocsis L., Salmi-Laouar S., Bosch D., Ameur-Zaimeche O., Foufou A. and Larit H. (2020) Comprehensive REE + Y and sensitive redox trace elements of Algerian phosphorites (Tébessa, eastern Algeria): A geochemical study and depositional environments tracking. *J. Geochem. Explor.* **208** 106396.

Kim J., Torres M. E., Haley B. A., Kastner M., Pohlman J. W., Riedel M. and Lee Y. (2012) The effect of diagenesis and fluid migration on rare earth element distribution in pore fluids of the northern Cascadia accretionary margin. *Chem. Geol.* **291**, 152–165.

Köbberich M. and Vance D. (2019) Zn isotope fractionation during uptake into marine phytoplankton: Implications for oceanic zinc isotopes. *Chem. Geol.* **523**, 154–161.

Kocsis L., Trueman C. N. and Palmer M. R. (2010) Protracted diagenetic alteration of REE contents in fossil bioapatites: Direct evidence from Lu–Hf isotope systematics. *Geochim. Cosmochim. Acta* **74**, 6077–6092.

Koeppenkastrop D. and De Carlo E. H. (1992) Sorption of rare earth elements from seawater onto synthetic mineral particles: an experimental approach. *Chem. Geol.* **95**, 251–263.

Kohn M. J., Schoeninger M. J. and Barker W. W. (1999) Altered states: effects of diagenesis on fossil tooth chemistry. *Geochim. Cosmochim. Acta* **63**, 2737–2747.

Krajewski K. P., Leśniak P. M., Łącka B. and Zawidzki P. (2000) Origin of phosphatic stromatolites in the Upper Cretaceous condensed sequence of the Polish Jura Chain. *Sediment Geol.* **136**, 89–112.

Kunzmann M., Gibson T. M., Halverson G. P., Hodgskiss M. S. W., Bui T. H. and Carozza D. A. (2017) Iron isotope biogeochemistry of neoproterozoic marine shales. *Geochim. Cosmochim. Acta* **209**, 85–105.

Kynicky J., Smith M. P. and Xu C. (2012) Diversity of Rare Earth Deposits: The Key Example of China. *Elements* **8**, 361–367.

Lécuyer C., Reynard B. and Grandjean P. (2004) Rare earth element evolution of Phanerozoic seawater recorded in biogenic apatites. *Chem. Geol.* **204**, 63–102.

Lécuyer C., Grandjean P., Barrat J., Nolvak J., Emig C., Paris F. and Robardet M. (1998) $\delta^{18}O$ and REE contents of phosphatic brachiopods: a comparison between modern and lower Paleozoic populations. *Geochim. Cosmochim. Acta* **62**, 2429–2436.

Li W., Czaja A. D., Van Kranendonk M. J., Beard B. L., Roden E. E. and Johnson C. M. (2013) An anoxic, Fe(II)-rich, U-poor ocean 3.46 billion years ago. *Geochim. Cosmochim. Acta* **120**, 65–79.

Li Z. X., Bogdanova S., Collins A., Davidson A., De Waele B., Ernst R., Fitzsimons I., Fuck R., Gladkochub D. and Jacobs J. (2008) Assembly, configuration, and break-up history of Rodinia: a synthesis. *Precambrian Res.* **160**, 179–210.

Liao J. L., Sun X. M., Li D. F., Sa R. N., Lu Y., Lin Z. Y., Xu L., Zhan R. Z., Pan Y. G. and Xu H. F. (2019) New insights into nanostructure and geochemistry of bioapatite in REE-rich deep-sea sediments: LA-ICP-MS, TEM, and Z-contrast imaging studies. *Chem. Geol.* **512**, 58–68.

Little S. H., Vance D., McManus J. and Severmann S. (2016) Key role of continental margin sediments in the oceanic mass balance of Zn and Zn isotopes. *Geology* **44**, 207–210.

Little S. H., Vance D., Walker-Brown C. and Landing W. M. (2014) The oceanic mass balance of copper and zinc isotopes, investigated by analysis of their inputs, and outputs to ferromanganese oxide sediments. *Geochim. Cosmochim. Acta* **125**, 673–693.

Liu X., Zhang H., Tang Y. and Liu Y. (2020) REE Geochemical Characteristic of Apatite: Implications for Ore Genesis of the Zhijin Phosphorite. *Minerals* **10**, 1012.

Liu Z. R. and Zhou M. (2017) Meishucun phosphorite succession (SW China) records redox changes of the early Cambrian ocean. *Geol. Soc. Am. Bull.* **129**, 1554–1567.

Liu Z. R. and Zhou M. (2020) Early Cambrian ocean mixing recorded by phosphorite successions in the Nanhua Basin, South China. *Precambrian Res.* **349** 105414.

Liu Y. S., Hu Z. C., Gao S., Günther D., Xu J., Gao C. G. and Chen H. H. (2008) In situ analysis of major and trace elements of anhydrous minerals by LA-ICP-MS without applying an internal standard. *Chem. Geol.* **257**, 34–43.

Lou F. J. and Gu S. Y. (2020) LA-ICP-MS REE analyses for phosphates and dolomites in Cambrian phosphorite in Zhijin, Guizhou Province: implication for depositional conditions and diagenetic processes. *J. Chin. Rare Earth Soc.* **38**, 225–239, In Chinese with English abstract.

Lumiste K., Mänd K., Bailey J., Paiste P., Lang L., Lepland A. and Kirsimäe K. (2019) REE+Y uptake and diagenesis in Recent sedimentary apatites. *Chem. Geol.* **525**, 268–281.

Mao T. and Yang R. D. (2013) Micro-structural characteristics and composition of the small shelly fossils in Cambrian phosphorites, Zhijin, Guizhou. *Acta Micropalaeontologica Sinica* **30**(2), 199–207, In Chinese with English abstract.

Mayer F., Apfelbaum F. and Featherstone J. D. B. (1994) Zinc ions in synthetic carbonated hydroxyapatites. *Arch. Oral Biol.* **39**, 87–90.

McArthur J. M. and Walsh J. N. (1984) Rare-earth geochemistry of phosphorites. *Chem. Geol.* **47**, 191–220.

Moeller K., Schoenberg R., Pedersen R., Weiss D. and Dong S. (2012) Calibration of the New Certified Reference Materials ERM-AE633 and ERM-AE647 for Copper and IRMM-3702 for Zinc Isotope Amount Ratio Determinations. *Geostand. Geoanal. Res.* **36**, 177–199.

Morel F., Reinfelder J. R., Roberts S. B., Chamberlain C. P., Lee J. G. and Yee D. (1994) Zinc and carbon co-limitation of marine phytoplankton. *Nature* **369**(6483), 740–742.

Nozaki Y., Zhang J. and Amakawa H. (1997) The fractionation between Y and Ho in the marine environment. *Earth Planet. Sci. Lett.* **148**, 329–340.

Okada Y., Sawaki Y., Komiya T., Hirata T., Takahata N., Sano Y., Han J. and Maruyama S. (2014) New chronological constraints for Cryogenian to Cambrian rocks in the Three Gorges, Weng'an and Chengjiang areas, South China. *Gondwana Res.* **25**, 1027–1044.

Ou Y. (2015) The research of occurrence state of rare-earth element in typical western Szechuan phosphate ore deposit. MA. Dissertation, Chengdu University of Technology, Chengdu, 1–56. (In Chinese with English abstract)

Pack A., Russell S. S., Shelley J. M. G. and van Zuilen M. (2007) Geo- and cosmochemistry of the twin elements yttrium and holmium. *Geochim. Cosmochim. Acta* **71**, 4592–4608.

Papineau D. (2010) Global biogeochemical changes at both ends of the proterozoic: insights from phosphorites. *Astrobiology* **10**, 165–181.

Paton C., Hellstrom J., Paul B., Woodhead J. and Hergt J. (2011) Iolite: freeware for the visualisation and processing of mass spectrometric data. *J. Anal. At. Spectrom.* **26**, 2508–2518.

Paul S., Volz J. B., Bau M., Köster M., Kasten S. and Koschinsky A. (2019) Calcium phosphate control of REY patterns of siliceous-ooze-rich deep-sea sediments from the central equatorial pacific. *Geochim. Cosmochim. Acta* **251**, 56–72.

Pi D., Liu C., Shields-Zhou G. A. and Jiang S. (2013) Trace and rare earth element geochemistry of black shale and kerogen in the early Cambrian Niutitang Formation in Guizhou province, South China: Constraints for redox environments and origin of metal enrichments. *Precambrian Res.* **225**, 218–229.

Piper D. Z. (1999) Trace elements and major-element oxides in the Phosphoria Formation at Enoch Valley, Idaho; Permian sources and current reactivities. Open-File Report.

Pokrovsky O. S., Viers J. and Freydier R. (2005) Zinc stable isotope fractionation during its adsorption on oxides and hydroxides. *J. Colloid. Interf. Sci.* **291**, 192–200.

Pons M. L., Fujii T., Rosing M., Quitté G., Télouk P. and Albarède F. (2013) A Zn isotope perspective on the rise of continents. *Geobiology* **11**, 201–214.

Reid R. P., M Ac Intyre I. G., Browne K. M., Steneck R. S. and Miller T. (1995) Modern marine stromatolites in the exuma cays, bahamas: uncommonly common. *Facies* **33**(1), 1–17.

Reynard B., Lécuyer C. and Grandjean P. (1999) Crystal-chemical controls on rare-earth element concentrations in fossil biogenic apatites and implications for paleoenvironmental reconstructions. *Chem. Geol.* **155**, 233–241.

Samanta M., Ellwood M. J. and Strzepek R. F. (2018) Zinc isotope fractionation by Emiliania huxleyi cultured across a range of free zinc ion concentrations. *Limnol. Oceanogr.* **63**, 660–671.

Sato T., Isozaki Y., Hitachi T. and Shu D. (2014) A unique condition for early diversification of small shelly fossils in the lowermost Cambrian in Chengjiang, South China: Enrichment of phosphorus in restricted embayments. *Gondwana Res.* **25**, 1139–1152.

Schoepfer S. D., Shen J., Wei H., Tyson R. V., Ingall E. and Algeo T. J. (2015) Total organic carbon, organic phosphorus, and biogenic barium fluxes as proxies for paleomarine productivity. *Earth-Sci. Rev.* **149**, 23–52.

Scholz F., Severmann S., McManus J. and Hensen C. (2014) Beyond the Black Sea paradigm: The sedimentary fingerprint of an open-marine iron shuttle. *Geochim. Cosmochim. Acta* **127**, 368–380.

Severmann S., Lyons T. W., Anbar A. D., McManus J. and Gordon G. (2008) Modern iron isotope perspective on the benthic iron shuttle and the redox evolution of ancient oceans. *Geology* **36**, 487–490.

Shields G. and Stille P. (2001) Diagenetic constraints on the use of cerium anomalies as palaeoseawater redox proxies: an isotopic and REE study of Cambrian phosphorites. *Chem. Geol.* **175**, 29–48.

Sieber M., Conway T. M., de Souza G. F., Hassler C. S., Ellwood M. J. and Vance D. (2020) Cycling of zinc and its isotopes across multiple zones of the Southern Ocean: Insights from the Antarctic Circumnavigation Expedition. *Geochim. Cosmochim. Acta* **268**, 310–324.

Sinoir M., Butler E. C. V., Bowie A. R., Mongin M., Nesterenko P. N. and Hassler C. S. (2012) Zinc marine biogeochemistry in seawater: a review. *Mar. Freshwater Res.* **63**, 644.

Steiner M., Li G., Qian Y., Zhu M. and Erdtmann B. (2007) Neoproterozoic to Early Cambrian small shelly fossil assemblages and a revised biostratigraphic correlation of the Yangtze Platform (China). *Palaeogeogr. Palaeoclimatol. Palaeoecol.* **254**, 67–99.

Swanner E. D., Wu W., Schoenberg R., Byrne J., Michel F. M., Pan Y. and Kappler A. (2015) Fractionation of Fe isotopes during Fe(II) oxidation by a marine photoferrotroph is controlled by the formation of organic Fe-complexes and colloidal Fe fractions. *Geochim. Cosmochim. Acta* **165**, 44–61.

Tang S. H., Zhu X. K., Cai J. J., Li S. Z., He X. X. and Wang J. H. (2006) Chromatographic separation of Cu, Fe and Zn using AGMP-1 anion exchange resin for isotope determination by MC-ICPMS. *Rock Miner. Anal.* **25**, 11–14, In Chinese with English abstract.

Tang S. H., Zhu X. K., Li J., Yan B., Li S. Z., Li Z. H., Wang Y. and Sun J. (2016) New standard solutions for measurements of iron, copper and zinc isotopic compositions using multi-collector inductively coupled plasma-mass spectrometry. *Rock Miner. Anal.* **35**, 127–133, In Chinese with English abstract.

Taylor S. R. and McLennan S. M. (1985) *The Continental Crust: Its Composition and Evolution. An Examination of the Geochemical Record Preserved in Sedimentary Rocks*. Blackwell Scientifc Publications, Oxford.

Vance D., Little S. H., Archer C., Cameron V., Andersen M. B., Rijkenberg M. J. A. and Lyons T. W. (2016) The oceanic budgets of nickel and zinc isotopes: the importance of sulfidic environments as illustrated by the Black Sea. *Philos. Trans. R. Soc. A* **374**, 20150294.

Veeramani H., Eagling J., Jamieson-Hanes J. H., Kong L., Ptacek C. J. and Blowes D. W. (2015) Zinc Isotope Fractionation as an Indicator of Geochemical Attenuation Processes. *Environ. Sci. Tech. Let.* **2**, 314–319.

Watkins R. T., Nathan Y. and Bremner J. M. (1995) Rare earth elements in phosphorite and associated sediment from the Namibian and South African continental shelves. *Mar. Geol.* **129**(1–2), 111–128.

Weber T., John S., Tagliabue A. and DeVries T. (2018) Biological uptake and reversible scavenging of zinc in the global ocean. *Science* **361**, 73–76.

Welch S. A., Beard B. L., Johnson C. M. and Braterman P. S. (2003) Kinetic and equilibrium Fe isotope fractionation between aqueous Fe and Fe(III). *Geochim. Cosmochim. Acta* **67**, 4231–4250.

Wen H. J., Carignan J., Zhang Y. X., Fan H. F., Cloquet C. and Liu S. R. (2011) Molybdenum isotopic records across the Precambrian-Cambrian boundary. *Geology* **39**, 775–778.

Wen H. J., Fan H. F., Zhang Y. X., Cloquet C. and Carignan J. (2015) Reconstruction of early Cambrian ocean chemistry from Mo isotopes. *Geochim. Cosmochim. Acta* **164**, 1–16.

Wu W., Swanner E. D., Kleinhanns I. C., Schoenberg R., Pan Y. and Kappler A. (2017) Fe isotope fractionation during Fe(II) oxidation by the marine photoferrotroph Rhodovulum iodosum in the presence of Si–Implications for Precambrian iron formation deposition. *Geochim. Cosmochim. Acta* **211**, 307–321.

Xiang L., Schoepfer S. D., Zhang H., Chen Z. W., Cao C. Q. and Shen S. Z. (2020) Deep-water dissolved iron cycling and reservoir size across the Ediacaran-Cambrian transition. *Chem. Geol.* **541** 119575.

Xiao C. Y., Zhang Z. W., He C. Z., Wen H. J. and Fan H. F. (2018) The depositional environment of Ediacaran phosphorite deposits, South China. Bull. Mineral. *Petrol. Geochem.* **37**, 121–138, In Chinese with English abstract.

Xing J., Jiang Y., Xian H., Zhang Z., Yang Y., Wei T., Liang X., Hecai N., Hongping H. e. and Zhu J. (2021) Hydrothermal activity during the formation of REY-rich phosphorites in the early Cambrian Gezhongwu Formation, Zhijin, South China: A micro- and nano-scale mineralogical study. *Ore Geol. Rev.* **136** 104244.

Xu L. G., Lehmann B., Mao J., Qu W. and Du A. (2011) Re-Os age of polymetallic Ni-Mo-PGE-Au mineralization in Early Cambrian Black Shales of South China-a reassessment. *Econ. Geol.* **106**, 511–522.

Yang X., Zhang Z., Santosh M., Duan S. and Liang T. (2018a) Anoxic to suboxic Mesoproterozoic ocean: Evidence from iron isotope and geochemistry of siderite in the Banded Iron Formations from North Qilian, NW China. *Precambrian Res.* **307**, 115–124.

Yang Y. H., Zhang X. C., Liu S. A., Zhou T., Fan H. F., Yu H. M., Chen W. H. and Huang F. (2018b) Calibrating NIST SRM 683 as a new international reference standard for Zn isotopes. *J. Anal. At. Spectrom.* **33**(10), 1777–1783.

Yasukawa K., Kino S., Azami K., Tanaka E., Mimura K., Ohta J., Fujinaga K., Nakamura K. and Kato Y. (2020) Geochemical features of Fe-Mn micronodules in deep-sea sediments of the western North Pacific Ocean: Potential for co-product metal extraction from REY-rich mud. *Ore Geol. Rev.* **127** 103805.

Yasukawa K., Liu H., Fujinaga K., Machida S., Haraguchi S., Ishii T., Nakamura K. and Kato Y. (2014) Geochemistry and mineralogy of REY-rich mud in the eastern Indian Ocean. *J. Asian Earth Sci.* **93**, 25–36.

Ye Y., Wang H., Wang X., Zhai L., Wu C. and Zhang S. (2020) Elemental geochemistry of lower Cambrian phosphate nodules in Guizhou Province, South China: An integrated study by LA-ICP-MS mapping and solution ICP-MS. *Palaeogeogr. Palaeoclimatol. Palaeoecol.* **538** 109459.

Ye Y., Wang H., Wang X., Zhai L., Wu C. and Zhang S. (2021) In situ rare earth element analysis of a lower Cambrian phosphate nodule by LA-ICP-MS. *Geol. Mag.* **158**, 749–758.

Zhang H. J., Fan H. F., Wen H. J., Zhu X. K. and Tian S. H. (2020) Oceanic chemistry recorded by cherts during the early Cambrian explosion, south china. *Palaeogeogr. Palaeoclimatol. Palaeoecol.* **558** 109961.

Zhang J., Amakawa H. and Nozaki Y. (1994) The comparative behaviors of yttrium and lanthanides in the seawater of the North Pacific. *Geophys. Res. Lett.* **21**, 2677–2680.

Zhang L., Algeo T. J., Cao L., Zhao L., Chen Z. Q. and Li Z. (2016) Diagenetic uptake of rare earth elements by conodont apatite. *Palaeogeogr. Palaeoclimatol. Palaeoecol.* **458**, 176–197.

Zhang W. (2016) Sedimentary character and metallogenic mechanism of stromatolitic phosphorite of Dengying Formation, Weng'an County of Guizhou Province, China. MA. Dissertation, Guizhou University, Guiyang, 1–80. (In Chinese with English abstract)

Zhang Z., Jiang Y., Niu H., Xing J., Yan S., Li A., Weng Q. and Zhao X. (2021) Enrichment of rare earth elements in the early Cambrian Zhijin phosphorite deposit, SW China: Evidence from francolite micro-petrography and geochemistry. *Ore Geol. Rev.* **138** 104342.

Zhao X., Zhang H., Zhu X., Tang S. and Yan B. (2012) Iron isotope evidence for multistage melt–peridotite interactions in the lithospheric mantle of eastern China. *Chem. Geol.* **292–293**, 127–139.

Zhu B., Jiang S., Yang J., Pi D., Ling H. and Chen Y. (2014) Rare earth element and Sr-Nd isotope geochemistry of phosphate nodules from the lower Cambrian Niutitang Formation, NW Hunan Province, South China. *Palaeogeogr. Palaeoclimatol. Palaeoecol.* **398**, 132–143.

Zhu M., Zhang J., Steiner M., Yang A., Li G. and Erdtmann B. (2003) Sinian-Cambrian stratigraphic framework for shallow- to deep-water environments of the Yangtze Platform: an integrated approach. *Prog. Nat. Sci.* **13**, 951–960.

Zhu R., Li X., Hou X., Pan Y., Wang F., Deng C. and He H. (2009) SIMS U-Pb zircon age of a tuff layer in the Meishucun section, Yunnan, southwest China: Constraint on the age of the Precambrian-Cambrian boundary. *Sci. China, Ser. D: Earth Sci.* **52**, 1385–1392.

*Associate editor:* Chao Li